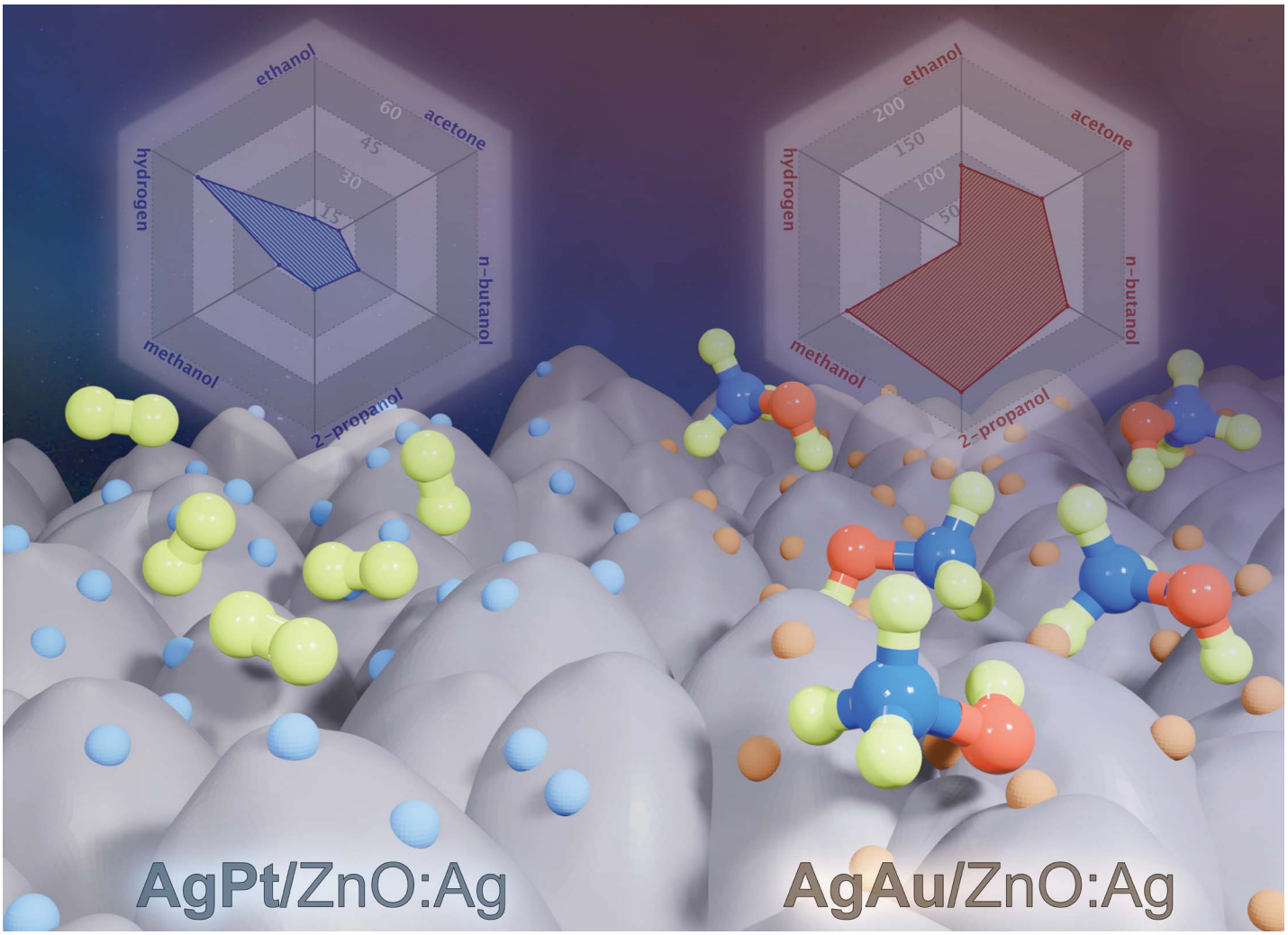

Highlighting work on the surface decoration of ZnO:Ag columnar thin films with AgAu and AgPt bimetallic alloy nanoparticles by a group of researchers around Prof. Franz Faupel, Prof. Lorenz Kienle and Prof. Rainer Adelung from Kiel University, Prof. Oleg Lupan from the Technical University of Moldova and Prof. Nora H. de Leeuw from the University of Leeds.

Surface functionalization of ZnO:Ag columnar thin films with AgAu and AgPt bimetallic alloy nanoparticles as an efficient pathway for highly sensitive gas discrimination and early hazard detection in batteries

Upon surface decoration with AgAu and AgPt nanoparticles, the gas sensing properties of columnar ZnO:Ag thin films were significantly enhanced. While the addition of AgAu nanoparticles resulted in an increase in gas response towards volatile organic compounds, the addition of AgPt nanoparticles efficiently changed the sensor selectivity to hydrogen gas.

As featured in:

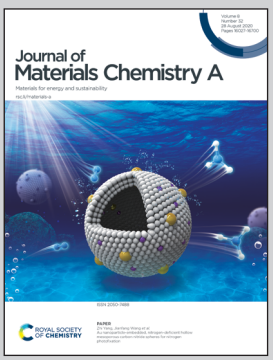

See David Santos-Carballal, Nora H. de Leeuw *et al.*, *J. Mater. Chem. A*, 2020, **8**, 16246.

ROYAL SOCIETY OF CHEMISTRY

rsc.li/materials-a

Registered charity number: 207890

Journal of Materials Chemistry A

ROYAL SOCIETY OF CHEMISTRY

PAPER

View Article Online
View Journal | View Issue

Cite this: J. Mater. Chem. A, 2020, 8, 16246

Surface functionalization of ZnO:Ag columnar thin films with AgAu and AgPt bimetallic alloy nanoparticles as an efficient pathway for highly sensitive gas discrimination and early hazard detection in batteries†

Alexander Vahl,[a] Oleg Lupan,[bc] David Santos-Carballal,[*de] Vasile Postica,[c] Sandra Hansen,[b] Heather Cavers,[b] Niklas Wolff,[f] Maik-Ivo Terasa,[b] Mathias Hoppe,[b] Abdelaziz Cadi-Essadek,[e] Torben Dankwort,[f] Lorenz Kienle,[f] Nora H. de Leeuw,[*dg] Rainer Adelung[b] and Franz Faupel[a]

For a fast and reliable monitoring of hazardous environments, the discrimination and detection of volatile organic compounds (VOCs) in the low ppm range is critically important, which requires the development of new chemical sensors. We report herein, a novel approach to tailor the selectivity of nanocomposite thin film sensors by investigating systematically the effect of surface decoration of Ag-doped ZnO (ZnO:Ag) columnar thin films. We have used AgPt and AgAu noble bimetallic alloy nanoparticles (NPs) to decorate the surfaces of ZnO:Ag and we have measured their resulting gas sensing properties towards VOC vapors and hydrogen gas. The gas response of the nanocomposite containing AgAu NPs to 100 ppm of ethanol, acetone, *n*-butanol, 2-propanol and methanol vapors was increased on average by a factor of 4 compared to the pristine ZnO:Ag columnar films. However, decoration with AgPt NPs led to a considerable reduction of the gas response to all VOC vapors and an increase of the response to H_2 gas by roughly one order of magnitude, indicating a possible route to tailor the selectivity by surface decoration. As such, the reported NP-decorated ZnO:Ag thin film sensors should be suitable for the detection of H_2 in Li-ion batteries, which is an early indication of the thermal runaway that leads to complete battery failure and possible explosion. To understand the impact of NP surface decoration on the gas sensing properties of ZnO:Ag thin films, we have employed density functional theory calculations with on-site Coulomb corrections and long-range dispersion interactions (DFT+*U*–D3-(BJ)) to investigate the adsorption of various VOC molecules and hydrogen onto the Ag-doped and NP-decorated ($10\bar{1}0$) surface of zinc oxide ZnO. The calculated surface free energies indicate that Ag_5Au_5/ZnO($10\bar{1}0$):Ag is the most favourable system for the detection of VOCs, which based on its work function is also the most reactive towards these species. Our calculated adsorption energies show that Ag_9Pt/ZnO($10\bar{1}0$):Ag has the largest preference for H_2 gas and the lowest preference for the organic adsorbates, which is in line with the high selectivity of AgPt/ZnO:Ag sensors towards the hydrogen molecule observed in our experiments.

Received 21st March 2020
Accepted 11th May 2020

DOI: 10.1039/d0ta03224g

rsc.li/materials-a

[a]Institute for Materials Science – Chair for Multicomponent Materials, Faculty of Engineering, Christian-Albrechts-University of Kiel, Kaiserstraße 2, D-24143 Kiel, Germany. E-mail: ff@tf.uni-kiel.de

[b]Institute for Materials Science – Functional Nanomaterials, Faculty of Engineering, Christian-Albrechts-University of Kiel, Kaiserstraße 2, D-24143 Kiel, Germany. E-mail: ra@tf.uni-kiel.de; ollu@tf.uni-kiel.de

[c]Center for Nanotechnology and Nanosensors, Department of Microelectronics and Biomedical Engineering, Technical University of Moldova, 168 Stefan cel Mare Av., MD-2004 Chisinau, Republic of Moldova. E-mail: oleg.lupan@mib.utm.md

[d]School of Chemistry, University of Leeds, Leeds LS2 9JT, UK. E-mail: D.Santos-Carballal@leeds.ac.uk; N.H.deLeeuw@leeds.ac.uk

[e]School of Chemistry, Cardiff University, Main Building, Park Place, Cardiff CF10 3AT, UK

[f]Institute for Materials Science – Synthesis and Real Structure, Faculty of Engineering, Christian-Albrechts-University of Kiel, Kaiserstraße 2, D-24143 Kiel, Germany

[g]Department of Earth Sciences, Utrecht University, Princetonplein 8A, 3584 CB Utrecht, The Netherlands. E-mail: n.h.deleeuw@uu.nl

† Electronic supplementary information (ESI) available. See DOI: 10.1039/d0ta03224g

Introduction

Nanocomposites that consist of noble metal nanoparticles (NPs) and micro- and nanostructures of semiconducting oxides, such as ZnO, SnO_2 and CuO, have attracted significant research interest for the their potentially sensitive detection of gases and VOC vapors,[1–8] owing to their excellent electronic, catalytic and optical properties.[8,9] Surface decoration by noble metal NPs has shown to affect many sensor characteristics including: (i) the sensitivity, enabling the detection of even trace amounts of gases; (ii) the selectivity towards certain gaseous species; (iii) the response and recovery times, which have been substantially reduced; and (iv) the acceptable operating temperatures, which have been shifted to values close to ambient conditions.[1,10–12] Recently, highly sensitive and selective hydrogen gas nanosensors have been described that are based on individual ZnO nanowires decorated by Pd NPs.[1,10] Guo *et al.* reported a remarkable enhancement of the gas sensing properties of ZnO nanorods by surface decoration with Au NPs, leading to fast response and recovery times, good selectivity and stable repeatability.[11,13] Majhi *et al.* have successfully prepared Au@ZnO core–shell NPs by a facile low-temperature solution route for highly selective H_2 gas detection, which was attributed to the chemical as well as catalytic effect of Au NPs.[12] Khan *et al.* have successfully sensitized NiO–ZnO heterostructures with Ag_2S by a cost-effective homogeneous precipitation method.[14]

However, recent results have demonstrated that bimetallic NPs have unique physico-chemical properties, superior to their monometallic counterparts, owing to the combination of their unique and the induced synergistic effects.[9,14–18] Yong *et al.* have used density functional theory calculations to investigate the adsorption of CO, HCN and NO on Ag_7Au_6 clusters for potential application as gas sensors and they found that adsorbates chemisorb on the surface of clusters with exothermic adsorption energies and finite charge transfer.[16] Choi *et al.* decorated SnO_2 nanowire networks with bimetallic PtPd NPs which led to fast response and recovery times during the detection of NO_2.[19] Fan *et al.* prepared ZnO loaded with PtAu bimetallic NPs, which showed high sensitivity to hydrogen down to the ppm-level, even at room temperature,[20] whereas Hassan *et al.* decorated ZnO nanorods with PtPd bimetallic core–shell NPs for accelerated hydrogen gas detection.[21]

Thus, it is crucially important to develop a technological approach which can control alloyed NP properties[15] and to investigate the gas sensing performance of decorated nanocomposites comprising micro- and nanostructured semiconducting oxides and bimetallic NPs. The Ag-based alloys, such as the bimetallic AgPt and AgAu NPs, are of particular interest due to the synergistic effect between the noble metal components, which makes them appealing for surface-enhanced Raman spectroscopy (SERS) as well as for applications in photocatalysis and sensing.[9,22,23] Ag-based NPs have several advantages compared to other noble metals, *e.g.*, harboring more active sites on their surface, which facilitates a more efficient electron transfer during the gas sensing applications.[22] Ag-containing NPs are also more cost-effective in their preparation than their monometallic counterparts.[22] The noble bimetallic AgAu NPs display a distinctive optical plasmon absorbance in the visible range.[24] Their monometallic components have very similar lattice constants (4.09 Å for Ag and 4.08 Å for Au), allowing the preparation of different core–shell structures as well as alloys down to an average diameter of 4–5 nm,[24] which are in high demand for device applications.

Despite their significant potential, the effect of AgAu and AgPt NPs decorating the surface of micro- and nanostructures of semiconducting oxides, especially columnar films, has not received much attention. Therefore, in the present study, nanocomposites were prepared by the decoration of Ag-doped ZnO columnar thin films (ZnO:Ag) with AgAu and AgPt NPs. Their gas sensing properties with regard to different VOCs and hydrogen gas were studied in detail. The sensors decorated with AgAu NPs-showed a significant increase in sensitivity towards VOCs compared to the pristine ZnO:Ag nanostructured films, whereas the sensors decorated using AgPt-displayed a change of selectivity from VOCs to H_2 gas.

Furthermore, we can place the concept of noble metal alloy NP nanocomposite sensors in the context of early hazard detection in Li ion batteries (LIB). In this particular application scenario, the fast and reliable detection of H_2 gas is especially important for the operation of battery modules that contain a large number of cells in parallel. The electrolytes are composed of a lithium salt and aprotic organic solvents, typically organic carbonates or ether solvents, which can produce H_2 gas as a decomposition product.[25–27] In this case, single battery cells inside a larger module experience degradation and a rise of their internal temperature to a critical point, which is likely to have a catastrophic effect on the performance of adjacent cells. In addition, in events like the sudden penetration or puncturing of the battery, the commonly used organic carbonate electrolytes decompose and produce large quantities of H_2 gas, alongside a temperature increase of up to 200–250 °C. Thus, there is urgent demand for an immediate detection system with the potential for direct integration into the individual cells to avoid failure of the complete battery. In this study, the high sensitivity and fast response times of AgPt NP nanocomposite sensors is related to a potential application in this scenario.

Finally, the corresponding gas sensing mechanisms are proposed and supported by an extensive theoretical investigation. To uncover the origin of the unique gas sensing properties of the bimetallic alloy NP-decorated ZnO:Ag thin films, first principles simulations were applied to study the sensing properties towards VOCs of the Ag-doped ZnO($10\bar{1}0$) surface decorated with Ag_5Au_5 and Ag_9Pt clusters, where the metal ratios were chosen for the simulations to reflect the similar composition of the experimentally obtained AgPt and AgAu NPs. The adsorption energies, electronic and structural implications have been investigated for different scenarios of substitutional doping and adsorption of the alloy metal clusters onto the surface. Furthermore, the binding of ethanol, acetone, *n*-butanol, 2-propanol, methanol and molecular hydrogen on the ZnO:Ag as well as the Ag_9Pt/ZnO:Ag and Ag_5Au_5/ZnO:Ag modified surfaces are discussed to account for changes in selectivity

and sensitivity. Whereas the sensitivity towards the VOC molecules was increased by the surfaces decorated with Ag_5Au_5 NPs, the Pt-based alloy NPs changed the nanocomposite's selectivity to H_2 gas, in correspondence with the experiment.

Experimental

Sample synthesis

Ag-doped ZnO nanostructured columnar thin films (ZnO:Ag) with a nominal thickness of ~1.5 μm were deposited on glass substrates by a simple and inexpensive synthesis method from chemical solutions (SCS). Details of the SCS method used to create the doped ZnO columnar films were presented in previous works.[28–31] The Ag doping content in the prepared samples was adjusted to 0.95 wt%, which was confirmed in an earlier investigation by energy-dispersive X-ray (EDX) spectroscopy and X-ray photoelectron spectroscopy (XPS).[32] All samples were thermally annealed at 650 °C for 2 h in air after deposition.

The noble bimetallic alloy NPs were deposited onto the ZnO:Ag columnar thin films and Si wafer pieces (for reference measurements, Si-Mat, 10 × 10 mm^2) using a custom-built high vacuum deposition system with an in-house Haberland type Gas Aggregation Source (GAS).[33–35] For the generation of the AgAu and AgPt bimetallic alloy NPs, customized silver targets (Kurt J. Lesker, 99.99%, 50.8 mm diameter) were used, with a drilled trench and a fitted Au wire (Alfa Aesar, 1.0 mm diameter, 99.95%) or Pt wire (Alfa Aesar, 1.0 mm diameter, 99.95%), respectively. The deposition of alloy NPs by applying the target geometry methodology has been characterized in detail in an earlier work.[36] A photograph depicting both targets in the geometry used is given in Fig. 1a, while the whole PVD setup is sketched in Fig. 1b. The respective target is mounted onto a DC planar magnetron source (Thin Film Consulting, ION'X-2UHV). Prior to deposition, the HV deposition system was evacuated to at least 10^{-4} Pa using a turbo molecular pump (Pfeiffer Vacuum, TMU 262) and a dry scroll pump (Agilent Technologies, SH-110). For sputtering, an Ar flow of 48 sccm, (purity 99.999%) was supplied at the gas inlet near the target (gas regulating valve: Pfeiffer, EVR116 with a hot ion cathode IMR 285 attached), resulting in a pressure of typically 136 Pa inside the GAS. For sputtering, a DC power of 40 W was supplied by the power source (Advanced Energy, MDX 500). Prior to every deposition, the target was cleaned and the NP growth was conditioned with a closed shutter for the time (at least 30 s) required to reach stable deposition conditions.

Sample characterization

Transmission Electron Microscopy (TEM) was used to investigate the nanostructure of the NP-decorated ZnO:Ag thin films using a Tecnai F30 G2 microscope (field emission gun, 300 kV) equipped with a Si(Li) EDX detector (EDAX system). TEM samples were prepared by scratching the nano–micro-columnar film containing the bimetallic clusters with a sharp knife and by subsequently transferring the resulting powder to a carbon lacey Cu grid by touching the grid onto the powder.

Analogous to previous works, for the electrical measurements, interdigitating Au electrodes were deposited by sputter deposition on top of the thin film.[29,37] The gas sensing properties were measured as reported previously.[28,38,39] Throughout this study, a typical concentration of 100 ppm of the respective gas species was applied to the gas sensors. To account for the low gas response of AgAu/ZnO:Ag and ZnO:Ag sensors towards hydrogen gas, the concentration in this test scenario was raised to 1000 ppm. The gas sensing properties were studied in a typical range of operating temperatures between 200 °C and 350 °C. The electrical measurements were performed using a Keithley 2400 SourceMeter, controlled by a LabView program (National Instruments).[37]

X-ray photoelectron spectroscopy (XPS, Omicron Nano-Technology GmbH, Al-anode, 240 W) was applied to investigate the chemical composition of the deposited NPs and nanocomposites. The C-1s line of adventitious carbon at roughly 285.0 eV was used for charge referencing of all recorded spectra. The software CasaXPS (version 2.3.16) was used to quantify the composition of the noble bimetallic AgAu and AgPt alloy NPs. Micro-Raman studies were performed at room temperature with a WITec alpha 300 RA system in backscattering configuration. The Nd-YAG laser power at the laser position was less than 4 mW.[39]

Calculation details

Density functional theory (DFT) calculations of the interaction of a number of VOCs and molecular hydrogen with the ZnO($10\bar{1}0$):Ag, Ag_5Au_5/ZnO($10\bar{1}0$):Ag and Ag_9Pt/ZnO($10\bar{1}0$):Ag decorated surfaces are also reported. All calculations were performed using the Vienna *Ab initio* Simulation Package

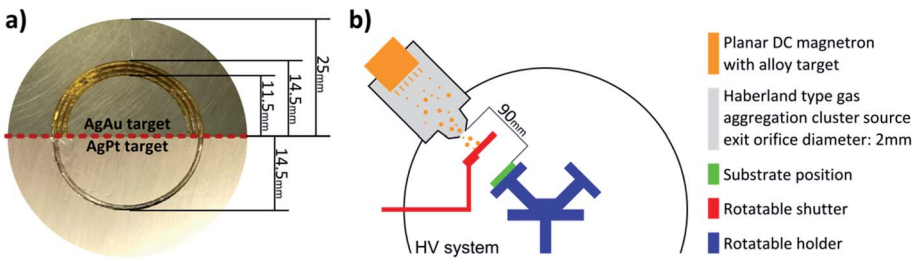

Fig. 1 (a) Photographic image of the AgAu (top half) and AgPt (bottom half) composite targets; (b) schematic illustration of the custom-built HV deposition system for deposition of noble bimetallic alloy NPs.

(VASP).[40–43] The valence electronic states were expanded *via* a plane-wave basis set with a kinetic energy cut-off of 400 eV. The projector augmented wave (PAW) method[44,45] was used to represent the interactions between the core (Au, Pt: [Xe] $4f^{14}$; Ag: [Kr]; Zn: [Ar]; O, C: [He]) and the valence electrons. For the H atoms, the electron was treated as valence. The method of Grimme with Becke–Johnson damping [D3-(BJ)][46,47] was applied to improve the description of the long-range dispersion forces. The simulations were carried out using the Perdew, Burke, and Ernzerhof (PBE)[48] exchange–correlation functional within the generalised gradient approximation (GGA). An effective U_{eff} value of 6.0 eV (ref. 39 and 49) was applied to the strongly correlated and localised Zn 3d electrons to enhance the description of their on-site Coulomb interactions.[50,51] However, no Hubbard Hamiltonian was employed for either the transition metal dopant or clusters states, as they are already delocalised given their low concentration[52] and metallic properties, respectively. The structures were optimised using the conjugate-gradients technique and were considered converged when the forces on all ions were less than 0.01 eV $Å^{-1}$. All calculations were spin-polarised to describe properly the unpaired electrons produced upon Zn(II) substitution by Ag(I).

The calculations of the insulating surfaces and isolated molecules were carried out sampling only the Γ point in the reciprocal space. However, the metallic phases were modelled using a Γ-centred Monkhorst–Pack mesh[53] with a maximum separation of 0.17 $Å^{-1}$ between *k*-points. The partial occupancies for the surfaces and isolated molecules were determined using the Gaussian smearing method,[54] with a width set at 0.05 eV. For the geometry optimisation of the metallic phases, the partial occupancies were simulated using the Methfessel–Paxton scheme order 1 with a smearing width of 0.10 eV. However, the tetrahedron method with Blöchl corrections was used for the static calculations of the metallic phases to simulate the magnetic and electronic properties and to obtain accurate total energies. These criteria allowed convergence of the total energy within 10^{-4} eV per atom.

Results and discussion

Morphological, structural and micro-Raman characterizations

SEM micrographs of pristine ZnO:Ag columnar thin films, as well as of nanocomposites decorated with AgAu and AgPt bimetallic alloy NPs, are depicted in Fig. 2. The morphology of a typical pristine ZnO:Ag thin film after heat treatment at 650 °C

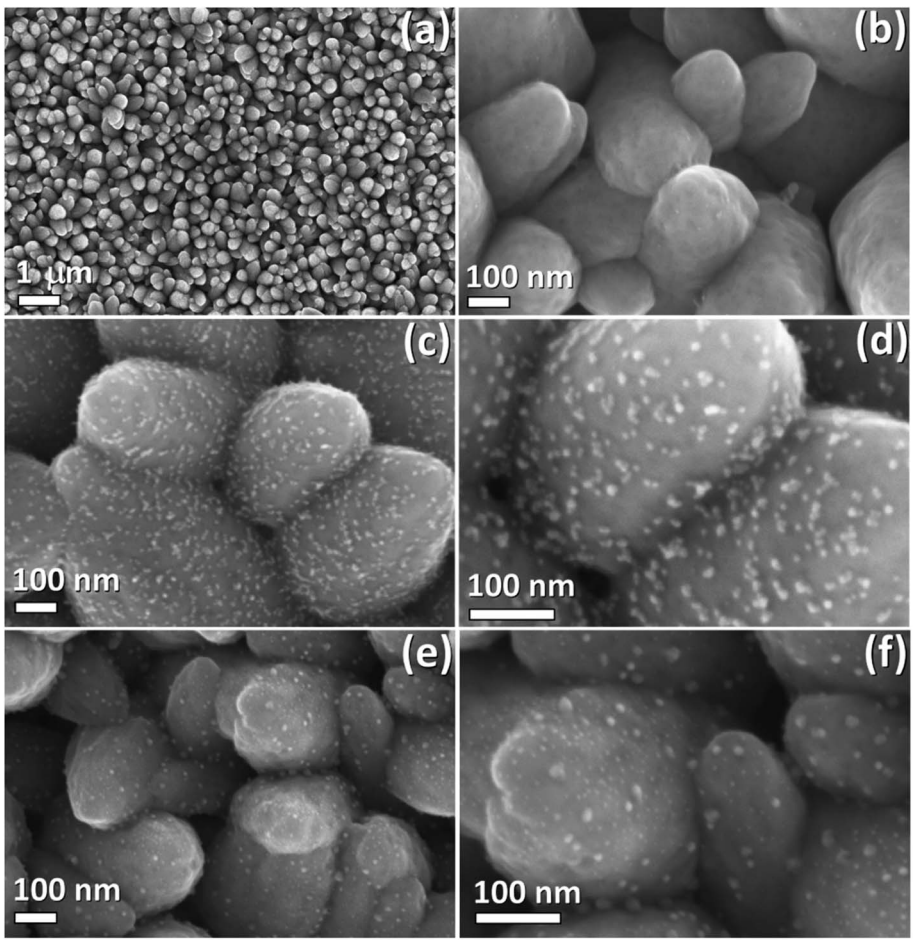

Fig. 2 SEM micrographs of ZnO:Ag columnar thin films after thermal annealing at 650 °C for 2 h: (a and b) pristine ZnO:Ag thin films; (c and d) ZnO:Ag thin films decorated by AgPt NPs; (d and e) ZnO:Ag thin films decorated by AgAu NPs.

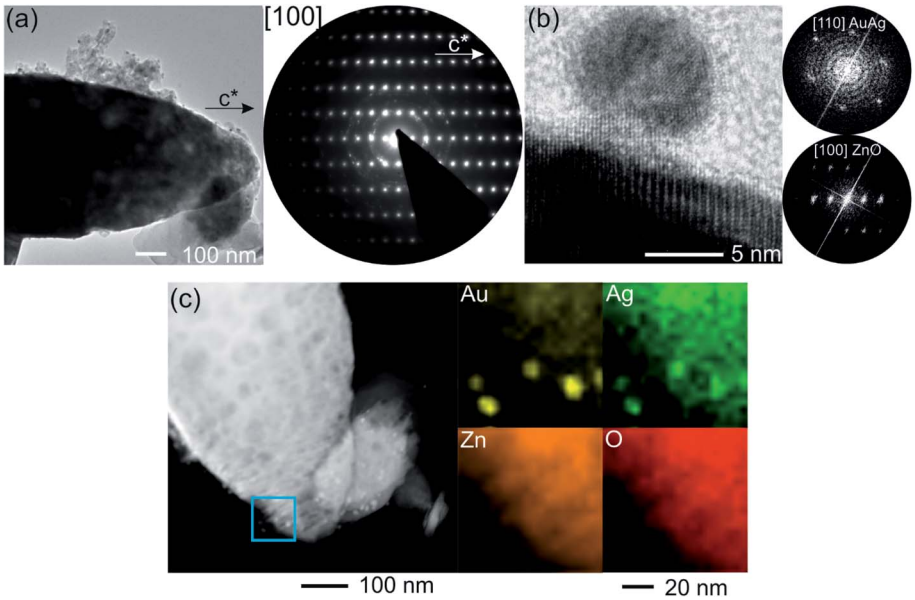

Fig. 3 (a) Overview TEM micrograph of a AgAu/ZnO:Ag nanocomposite: electron diffraction pattern of the tip of the AgAu/ZnO:Ag nanostructure verify that these are single crystalline structures and exhibit a *c*-axis growth direction. (b) HRTEM of a AgAu NP attached to the surface of the AgAu/ZnO:Ag nanostructure and corresponding FFT. (c) EDX elemental mapping of the marked region indicates the presence of AgAu alloy NPs.

for 2 h (Fig. 2a and b) consists of closely packed and partially interconnected grains. The diameter of these grains varies between 50 and 400 nm. SEM micrographs of ZnO:Ag columnar thin films, which were decorated with AgPt NPs, are displayed in Fig. 2c and d. The bimetallic AgPt NPs have a diameter ranging between 5 and 15 nm and are well distributed on the surface of the ZnO:Ag columnar thin films, showing no formation of percolating paths. However, due to the stochastic character of the deposition method, occasional agglomeration of small numbers of NPs is observed (see Fig. 2d). The SEM micrographs showing ZnO:Ag thin films decorated by AgAu NPs are presented in Fig. 2e and f. In this case, the deposited NPs exhibit typical NP diameters between 3 nm and 18 nm (see Fig. 2f). In both AgPt and AgAu alloy NPs, the mean diameter is considerably smaller than the grain diameter of the ZnO:Ag thin film. These observed diameters, as well as the sparse deposition with occasional agglomerations, agrees well with a typical NP deposition *via* GAS well below the percolation threshold.[36]

Moreover, TEM experiments were conducted to investigate the nanostructure and verify the presence of bimetallic alloy NPs. For example, Fig. 3a depicts an overview image of an AgAu/ZnO:Ag nanocomposite. The electron diffraction (ED) pattern, recorded at the tip of the displayed AgAu/ZnO:Ag grain, provides information that the doped columnar grains grow as single crystals along the *c*-axis of the wurtzite-type structure. Furthermore, the ED pattern exhibits weaker diffraction intensities distributed on rings. The appearance of these rings is attributed to polycrystalline ZnO, which is partially adhered to the surface and alloy NPs. High resolution TEM micrographs (see Fig. 3b) show the presence of NPs with diameters in the range of 5–20 nm, which is in good agreement with the observations from the SEM micrographs of Fig. 2f. The imaged NPs seem to be loosely bound to the ZnO surface and do not show a systematic intergrowth structure. The Fourier transform of the matrix verifies the presence of a single crystalline ZnO (zone axis [100], [21−10] in hexagonal notation) phase. Due to the similar crystal structures of Ag and Au, the composition of the NPs could not be distinguished between the pure metals or alloy (zone axis [110]). To verify the presence of AgAu NPs (or AgPt NPs), the nanocomposite was investigated by EDX elemental mapping (see Fig. 3c or S2,† respectively). The EDX elemental map (Fig. 3c) clearly shows the location of the overlapped signals for the high Ag and Au, which indicates the presence of AgAu alloy NPs. A similar trend is observed in the EDX signals for Ag and Pt in the AgPt/ZnO:Ag nanocomposite (Fig. S2†). It is reported that Ag and Pt form a miscibility gap ranging roughly from 13 at% to 98 at%, with respect to Pt content.[55,56] However, phase separation could not be identified within the measuring limits of the microscope used (Fig. S2†). Considering that Pt content is about 12 at% (see XPS studies below), it is reasonable to assume that a solid solution has formed.

Fig. S1† shows the Raman spectra of the AgAu- and AgPt-decorated ZnO:Ag columnar films. For all samples, the two dominant peaks were observed at ~100 cm^{-1} and ~438 cm^{-1}, which are attributed to the E_2(low) and E_2(high) modes of the wurtzite structure of ZnO, respectively. Other peaks with lower intensities were observed at ~337, ~380, ~410, ~576 and ~584 cm^{-1}, which are attributed to E_2(high)–E_2(low), A_1(TO), E_1(TO), A_1(LO) and E_1(LO) modes, respectively.[30,31]

XPS studies

The ZnO:Ag nanocolumnar thin film (as a reference layer), as well as the nanocomposites decorated with the AgPt and AgAu

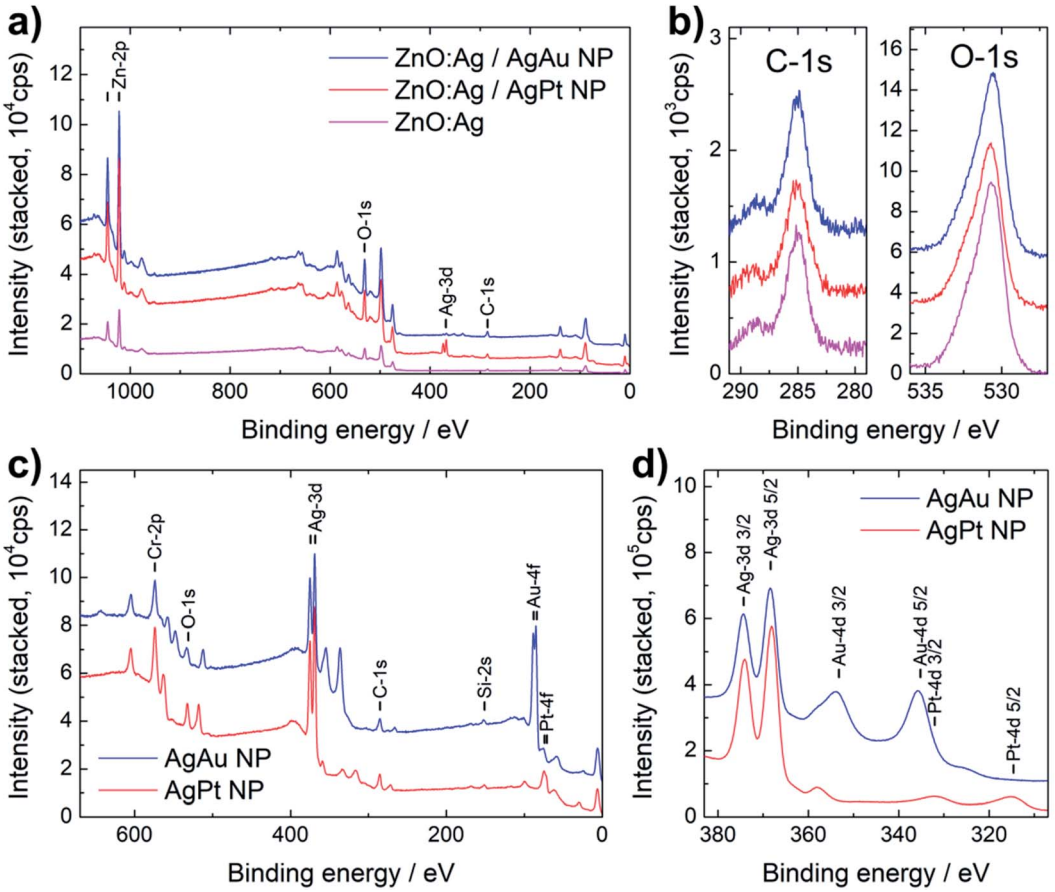

Fig. 4 (a) Overview XPS spectra of ZnO:Ag columnar thin film (magenta line) and nanocomposites with AgAu (blue line) and AgPt (red line) bimetallic alloy nanoparticles; (b) high resolution spectra of C-1s and O-1s lines; (c) XPS spectra of AgAu alloy NP layers (blue line) and AgPt (red line) for overview; and (d) detailed quantification of nanoparticle composition.

alloy NPs, were investigated by XPS. Fig. 4a shows the overview spectra of the nanocomposites (AgAu: red line, AgPt: blue line) and the reference layer (magenta, bottom line). Based on the characteristic peaks of these spectra, the elemental composition is determined. The elements Zn, O, C and Au are detected in all spectra. The position of line C-1s in Fig. 4b, which was used for charge referencing, indicates atmospheric surface contamination from organic compounds, such as carbohydrates.[32] The prominent signal of Zn and O is attributed to the ZnO base layer. The comparison of the O-1s high resolution spectra (Fig. 4b) indicates a similar peak position and shape for the investigated nanocomposites as well as for the pristine substrate. Ag is detected in all three samples, but the corresponding signal is rather weak, especially for the ZnO:Ag base layer, which is attributed to the low doping concentration of Ag. A comparison of high resolution spectra of the Ag-3d, Au-4d and Pt-4d lines can be found in Fig. S3.† The signal is stronger in the case of the AgAu NPs and AgPt NPs decorated nanocomposites, but due to the intentionally low surface coverage of NP, the signal is still weak for a precise quantification.

For further investigation of the deposited NPs, the reference spectra of AgPt and AgAu alloy NPs (deposited on silicon wafer pieces) are compared in Fig. 4c and d. The overview spectra in Fig. 4c indicates the presence of Si, Cr, O, C, Ag and Au or Pt for the AgAu and AgPt NPs, respectively. To quantify the composition of the bimetallic alloy NPs, a detailed binding energy scan of the Ag-3d, Au-4d and Pt-4d lines from 382 eV to 313 eV is shown in Fig. 4d. Additional peaks with an offset to lower binding energies (by roughly 10 eV) occur in the spectra, due to the use of a non-monochromated X-ray source. In case of the AgAu NPs, the offset peak from Ag-$3d_{5/2}$ overlaps with the Au-$4d_{3/2}$ line. Accordingly, the Au-4f line was used for the quantification of Au, which was estimated at 52 at% in the AgAu NPs. For the AgPt NPs, the relevant Ag-3d and Pt-4d lines are well separated and correspond to a Pt content of roughly 12 at%. Considering the lower sputtering rate of Pt compared to Au (roughly 0.57 of Au) and the difference in target design (three Au wires for AgAu and one Pt wire for AgPt), the difference in concentration of Ag in the AgPt and AgAu NPs is expected.[33–36] The estimated composition of AgPt and AgAu NPs is presented in Table S1 in the ESI.†

Gas sensing properties

Fig. 5a shows the gas response of the pristine ZnO:Ag, AgPt/ZnO:Ag and AgAu/ZnO:Ag nanocomposites to hydrogen gas (H_2) and different VOC vapors, including ethanol, acetone, *n*-

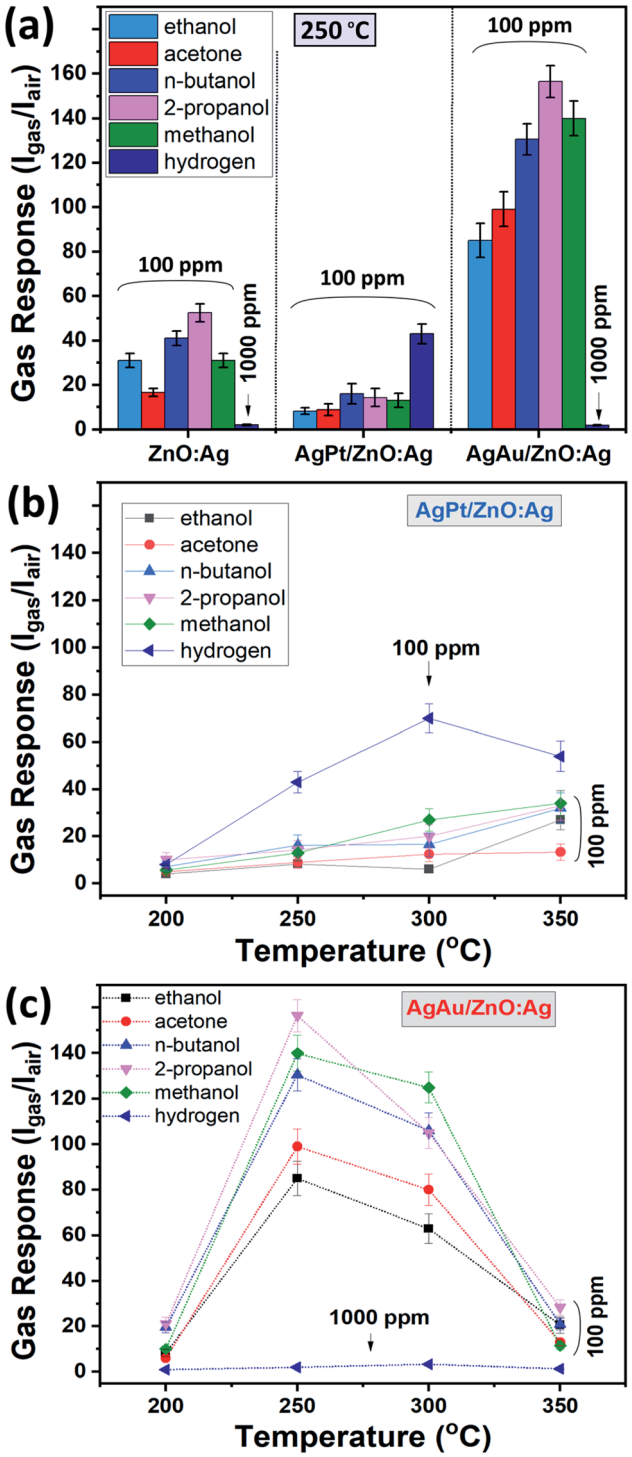

Fig. 5 (a) Gas response to H_2 gas and different VOC vapors for ZnO:Ag, AgPt/ZnO:Ag and AgAu/ZnO:Ag columnar films at 250 °C operating temperature. The concentration of VOC vapors is 100 ppm. The concentration of H_2 gas is 100 ppm for the highly responsive AgPt/ZnO:Ag composite while it is 1000 ppm for the pristine ZnO:Ag thin film and AgAu/ZnO:Ag composite. Temperature dependence of the gas response for the AgPt/ZnO:Ag (b) and AgAu/ZnO:Ag (c) nanocomposite.

butanol, 2-propanol and methanol at an operating temperature of 250 °C. In a typical gas sensing experiment, the thin film sensor was exposed to a concentration of 100 ppm of each VOC or H_2. However, in the case of the ZnO:Ag and AgAu/ZnO:Ag columnar films, an H_2 concentration of 1000 ppm was used to underline the low sensitivity of these sensors towards H_2. A considerable increase of the response to VOC vapors was observed for the ZnO:Ag columnar films that were decorated with AgAu NPs. The gas response of the ZnO:Ag columnar films to 1000 ppm of hydrogen and 100 ppm of ethanol, acetone, *n*-butanol, 2-propanol and methanol is ~2.1, ~31, ~16.5, ~41, ~52.5 and ~31, respectively, while for AgAu/ZnO:Ag it is ~2, ~85, ~99, ~130.5, ~156.5 and ~140, respectively. Compared to the pristine ZnO:Ag thin film, the gas response of AgAu/ZnO:Ag to ethanol, acetone, *n*-butanol, 2-propanol and methanol was increased by factor of ~2.8, ~6, ~3.2, ~3 and ~4.5, respectively. The gas response values are also considerably higher compared to those obtained for ZnO:Ag columnar films decorated with monometallic Ag NP-synthesized by the same method,[32] proving the higher efficiency of bimetallic NP decoration. The low gas response to hydrogen gas is characteristic for all samples, with the exception of the AgPt/ZnO:Ag columnar films. Although the decoration with the AgPt alloy NPs leads to a decrease in response for all the VOCs tested, by a factor of 2, it enhances the sensitivity to 100 ppm of H_2 gas by a factor 40. This is a large change compared to the almost no response to H_2 gas in the case of the reference and the AgAu decorated sample sets, which indicates the possibility of tailoring the selectivity of ZnO:Ag thin film sensors by surface decoration with noble bimetallic alloy NPs of various composition. In addition to contemporary approaches, *e.g.* incorporating molecular sieves,[57] the versatility of GAS to produce a variety of metal, metal alloy and metal oxide NPs opens up a highly interesting research field for further improvements in sensor selectivity.

Fig. 5b and c show the dependence of the gas response, to H_2 and different VOC vapors with respect to the operating temperature for the AgPt/ZnO:Ag and AgAu/ZnO:Ag nanocomposites, respectively. In both cases, the optimal operating temperature is 250–300 °C. Since no gas response higher than 1.5 was observed at operating temperatures below 200 °C, this temperature regime was not investigated further.

The dynamic response of the AgPt/ZnO:Ag columnar films to 100 ppm of H_2 gas at different operating temperatures (200–350 °C) is presented in Fig. 6a. The calculated values for the associated response and recovery times are presented in Fig. 6b. The response times are confined to a small range (11–20 s), while the recovery times decrease from 36 s to 10 s when the operating temperature rises from 200 to 350 °C.

The dependence of the H_2 gas response (S_{H_2}) to its concentration at 250 and 300 °C is presented in Fig. 6c. A power law relationship is observed ($S_{H_2} \propto p_{H_2}^{\beta}$), where β, which is the slope of log S_{H_2} *vs.* log p_{H2},[39] has a value of $\beta \approx 0.85$ at both 250 and 300 °C. The detection limits calculated for the H_2 gas (criterion for gas detection: $I_{gas}/I_{air} > 1.2$ (ref. 58)) were ~1 and ~0.6 ppm at 250 and 300 °C, respectively.

The dynamic responses of the AgAu/ZnO:Ag columnar films to 100 ppm of VOC vapors at their optimal operating temperatures of 250 °C are presented in Fig. 6d. All samples show fast signal recovery to the initial electrical baseline after evacuation of the vapors from the test chamber, which is essential for the

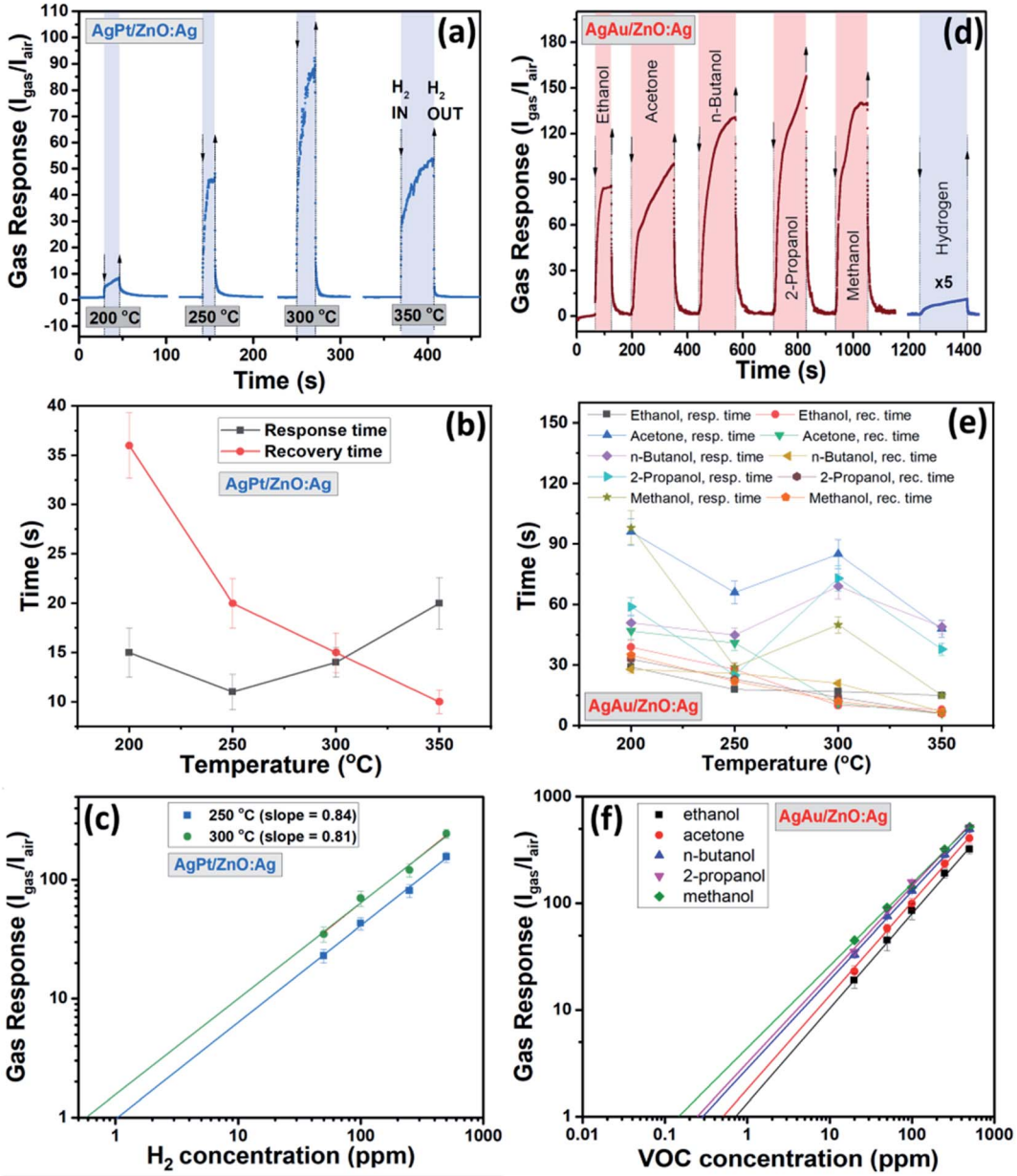

Fig. 6 (a) Dynamic response of a AgPt/ZnO:Ag nanocomposite sensor to 100 ppm of H_2 gas at different operating temperatures (200–350 °C). (b) The response and recovery times of a AgPt/ZnO:Ag nanocomposite-based sensor to 100 ppm of H_2 gas *versus* operating temperature. (c) The dependence of H_2 gas response to H_2 gas concentration for AgPt/ZnO:Ag films-based sensor at 250 and 300 °C. (d) Dynamic response of a AgAu/ZnO:Ag nanocomposite-based sensor to 100 ppm of VOC vapors and 1000 ppm of H_2 gas at 250 °C. (e) Response and recovery times of a AgAu/ZnO:Ag nanocomposite sensor *versus* operating temperature for different VOCs. (f) Dependence of gas response to the concentration of VOC vapours for AgAu/ZnO:Ag films-based sensor at 250 °C of operating temperature.

reliability of sensors and their practical applications. The calculated response and recovery times *versus* the operating temperature are presented in Table 1 and Fig. 6e. The recovery times for all samples are comparable to one of the best results reported for functionalized/decorated ZnO samples (see Table 2).

Table 2 shows other results for high performance VOC vapors sensors based on ZnO micro- and nanostructures functionalized/decorated/modified with monometallic and noble bimetallic (Au, Ag, Pt) NPs. This table clearly demonstrates that our results are equivalent or superior to the performances reported for highly sensitive VOC sensors, although there are several reports of H_2 response values much higher than for our AgPt/ZnO:Ag columnar films.[1,10,59–61] However, the remarkable point of our materials is the possibility to change the selectivity from VOC vapors to H_2 gas, which opens the opportunity for the fabrication of highly selective gas sensors. In addition, the platinum content in the bimetallic AgPt NPs, which in this work was determined to be roughly 12

Table 1 Overview over of the calculated response and recovery times to VOC vapors at different operating temperatures

			Temperature, °C			
			200	250	300	350
ZnO:Ag	Ethanol	Resp. time (s)	62	49	22	18
		Rec. time (s)	16	9	3	2
	Acetone	Resp. time (s)	114	65	41	18
		Rec. time (s)	47	11	3	2
	n-Butanol	Resp. time (s)	88	105	43	38
		Rec. time (s)	22	10	4	3
	2-Propanol	Resp. time (s)	57	65	38	24
		Rec. time (s)	16	6	4	3
	Methanol	Resp. time (s)	80	51	17	40
		Rec. time (s)	28	10	4	3
AgPt/ZnO:Ag	Hydrogen	Resp. time (s)	15	11	14	20
		Rec. time (s)	36	20	15	10
	Acetone	Resp. time (s)	78	21	29	20
		Rec. time (s)	36	11	5	3
	n-Butanol	Resp. time (s)	61	6	28	8
		Rec. time (s)	29	7	5	3
	2-Propanol	Resp. time (s)	113	94	43	40
		Rec. time (s)	43	15	3	2
	Methanol	Resp. time (s)	46	23	45	34
		Rec. time (s)	32	8	4	2
AgAu/ZnO:Ag	Ethanol	Resp. time (s)	29	18	17	15
		Rec. time (s)	39	28	10	8
	Acetone	Resp. time (s)	96	66	85	48
		Rec. time (s)	47	41	11	6
	n-Butanol	Resp. time (s)	51	45	69	49
		Rec. time (s)	28	26	21	7
	2-Propanol	Resp. time (s)	59	25	73	38
		Rec. time (s)	33	23	14	6
	Methanol	Resp. time (s)	98	29	50	15
		Rec. time (s)	35	22	12	6

at%, results in a more cost-effective approach to tailor the sensor selectivity compared to the use of the pure material.

The dependence of the gas response on the concentration of VOC vapors for the AgAu/ZnO:Ag columnar films is presented in Fig. 6f. For ethanol, acetone, *n*-butanol, 2-propanol, and methanol the β value is $\approx$0.87, 0.88, 0.83, 0.82, and 0.78, respectively, whereas the estimated detection limit for ethanol, acetone, *n*-butanol, 2-propanol, and methanol are $\sim$1, 0.8, 0.5, 0.4, 0.3 and 0.2 ppm, respectively.

Alloy NP-decorated thin film gas sensors as candidate materials for monitoring thermal runaway in Li-ion-batteries

From the gas sensing studies, it can be concluded that the surface decoration of the ZnO:Ag columnar films with AgAu NPs increases the selectivity to VOC vapors, while the surface decoration using AgPt NPs changes the response and leads to high selectivity to hydrogen gas. Thus, the selectivity of the ZnO:Ag films can be easily tuned using bimetallic NPs of different composition for surface decoration of the columns, which is of significant interest for gas sensing applications. In view of the versatility in tailoring the sensor's selectivity, and taking into account its fast response and recovery times, the alloy NP-decorated ZnO:Ag thin film sensors are highly promising materials for early hazard detection in LIBs, where many of the decomposition products, especially from the electrolyte solvents, are extremely flammable.[25,27] Hazard detection in LIBs is especially demanding, as thermal runaway in a malfunctioning cell can rapidly destroy the whole device and other neighboring components, leading to a complete failure of all individual cells. For critical applications *e.g.* in the automotive sector, each cell should be equipped with a fast and robust hazard detection system in order to prevent fire spreading to other cells.

In the case of thermal runaway, the LIB heats to over 200 °C and produces large amounts of H_2 gas. Applying the alloy NP/ZnO:Ag thin film sensors in close vicinity of each battery cell would allow the identification of failing units as the H_2 gas produced can be detected, whereas the thermal runaway provides the appropriate operating temperature for the sensor. Accordingly, the sensitivity of the AgPt/ZnO:Ag sensor towards H_2 would be enhanced as the temperature is raised, making this decorated surface an excellent material for the detection of thermal runaway in LIB. In contrast, the AgAu/ZnO:Ag sensor has a significantly lower response towards H_2 gas and is therefore an effective material to rule out sensor malfunction.

Thus, the integration of alloy NP/ZnO:Ag thin film sensors into individual battery cells is a potential pathway to achieve a cost effective and fast detection method of the early stages of thermal runaway, and to avoid the deterioration of other cells connected in parallel.

Gas sensing mechanism for bimetallic alloy NP-decorated films

The gas sensing mechanism of the decorated columnar films can be explained by changes in the electronic and chemical sensitization effects, *i.e.* the formation of nano-Schottky barriers at the interface between ZnO:Ag and the AgPt and AgAu alloy NPs,[2,3,62] as well as the catalytic properties of the bimetallic NPs. Given that the diameter of the ZnO:Ag grains is larger than its Debye length, the nano-Schottky barriers formed at the Au/ZnO:Ag and Pt/ZnO:Ag interface have a low impact on the improvement of the gas sensing properties.[10,63] Moreover, from the observation that ZnO:Ag columnar thin films decorated with AgPt and AgAu NPs exhibit very different sensing properties, it can be concluded that the chemical sensitization is the dominant effect (*i.e.* the catalytic properties of the bimetallic NPs). Choi *et al.* demonstrated that surface decoration of CuO NWs with different types of NPs, by modification of the conduction channel width, does not change the selectivity of the material.[63] Therefore, the excellent catalytic properties of Pt towards the adsorption and dissociation of hydrogen is the key parameter that explains the change of selectivity by surface decoration with AgPt NPs.[20] A number of studies have demonstrated that the addition of Pt NPs to different nano- and microstructures of metal oxides can greatly enhance the response to H_2 gas.[20,21,64–66] The Pt NPs may provide more active sites than any other noble metal for the adsorption and catalytic dissociation of oxygen species and H_2 molecules.[20,66] During the sensing process, the spillover and oxidation of hydrogen

Table 2 Comparison of the sensing properties for VOC and H_2 sensors based on metal oxides modified/decorated with different noble metals

Sensing material	VOCs conc. (ppm)	Gas response (I_{gas}/I_{air}) or (R_{air}/R_{gas})	Operating temperature (°C)	Response time (s)	Recovery time (s)
Ag–ZnO films[84]	Ethanol 2000	~2	225	5	—
Ag/ZnO nanorods[85]	Ethanol 100	36.52	360	50	28
ZnO–Ag hybrids[86]	Ethanol 100	101.8	370	~15	~20
Ag–ZnO nanorods[87]	Ethanol 50	34.8	280	—	—
	Acetone 50	25			
	Methanol 50	14.5			
Ag-loaded ZnO[88]	Ethanol 100	~75	240	—	—
	Acetone 100	~30			
	Isopropanol 100	~68			
	Methanol 100	~55			
Au-doped ZnO NWs[89]	Ethanol 1000	~37	240	—	—
Au/ZnO NWs[11]	Ethanol 100	33.6	380	3	1
Au/ZnO nanorods[90]	Ethanol 100	89.5	300	2	2
Au NPs/ZnO[91]	Ethanol 1000	32	300	—	—
Au/ZnO nanoplates[77]	Ethanol 100	21	400	2	2
	Acetone 100	32		4	4
Au/ZnO nanoplates[92]	Ethanol 100	20	300	13	—
	Acetone 100	16		—	—
	Methanol 100	7		—	—
Au/ZnO yolk–shell nanospheres[70]	Acetone 100	37	300	2	38
	Methanol 100	~22		—	—
Au/ZnO[71]	Ethanol 50	8.9	300	10	—
	Methanol 50	~7			
Au@ZnO core–shell nanoparticles[12]	Ethanol 100	~63	300	75	600
Au/T-TiZnO[93]	Ethanol 50	~22	320	—	—
Au/flower-like ZnO[69]	Ethanol 100	45.56	270	—	—
	Acetone 100	74.41		5	3
Pt/ZnO NWs[94]	Ethanol 50	32.6	265	—	—
PtAu/ZnO nanorods[20]	H_2 250	~160	130	—	—
PtPd/ZnO nanorods[21]	H_2 10 000	~3	100	5	76
AgPt/ZnO:Ag columnar films (this work)	**H_2 100**	**43**	**250**	**11**	**20**
		70	**300**	**14**	**15**
	Ethanol 100	8.3	250	7	12
	Acetone 100	8.9	250	21	11
	2-Propanol 100	14.3	250	6	7
	n-Butanol 100	16.2	250	94	15
	Methanol 100	13	250	23	8
AgAu/ZnO:Ag columnar films (this work)	Ethanol 100	85	**250**	18	28
	Acetone 100	99		66	41
	2-Propanol 100	**156.5**		**45**	**26**
	n-Butanol 100	130.5		25	23
	Methanol 100	140		29	22
	Hydrogen 1000	2		64	21

molecules by the adsorbed oxygen species (see eqn (1)) located near the AgPt bimetallic NPs, explains the high response to H_2 gas.[21,66] Taking into account the low concentration of roughly 12% of Pt in our AgPt bimetallic NPs, the strong shift of selectivity towards H_2 gas is even more remarkable.

$$2O^-_{(ads)} + 2H_2 \rightarrow 2H_2O + 2e^- \quad (1)$$

Liu *et al.* also observed that the addition of Pt NPs to SnO_2 leads to considerable decrease in the response to VOC vapors, while the addition of Au NPs induces the opposite effect.[20,66] These findings also support the large effect of the chemical sensitization on the gas sensing properties and selectivity of the AgPt/ZnO:Ag columnar films towards H_2 gas. Another mechanism which can explain the high selectivity of the AgPt/ZnO:Ag samples is the formation of PtH_x species at the relatively high operating temperatures of 250–300 °C. Under these conditions, the number of hydrogen atoms per Pt site increases, and the metal becomes a better catalyst for hydride formation.[21]

For the AgAu/ZnO:Ag columnar films, the greatly enhanced sensing properties towards VOCs can be explained by the excellent catalytic properties of the Au component of the NPs towards the dissociation of oxygen and the (partial) oxidation of the VOC molecules.[20,66–69] The Au NPs will provide more active

sites for the adsorption of oxygen species than the pristine surface of ZnO.[70] Many studies have demonstrated that the addition of Au NPs to nano- and microstructures of metal oxides leads to an enhancement in the overall response and selectivity to VOC vapors.[67–71] The proposed reaction for the oxidation of the VOC molecules by the adsorbed oxygen species can be described as follows:[11,70,72–74]

$$\text{(Acetone) } CH_3COCH_3 + 8O^- \leftrightarrow 3CO_2 + 3H_2O + 8e^- \quad (2)$$

$$\text{(Ethanol) } C_2H_5OH + 6O^- \leftrightarrow 2CO_2 + 3H_2O + 6e^- \quad (3)$$

$$\text{(Methanol) } CH_3OH + O^- \leftrightarrow HCHO + H_2O + e^- \quad (4)$$

$$\text{(2-Propanol) } C_3H_7OH + O^- \rightarrow (CH_3)_2CO + H_2O + e^- \quad (5)$$

$$\text{(}n\text{-Butanol) } C_4H_9OH + 12O^- \rightarrow 4CO_2 + 5H_2O + 12e^- \quad (6)$$

The high response to 2-propanol, compared to other VOC vapors, can be explained by the presence of methyne (CH) groups, which are essential for a more efficient decomposition and oxidation of this molecule.[75,76] The general reaction can be described as:[77]

$$VOC + nO^- \rightarrow aCO_2 + bH_2O + ne^- \quad (7)$$

Calculated properties

The DFT calculations have been performed to gain insight into the physio-chemical properties of the gas molecules (CH_3CH_2-OH, CH_3COCH_3, n-C_4H_9OH, 2-C_3H_7OH, CH_3OH and H_2) adsorbed on the Ag-doped ZnO(10$\bar{1}$0) surface decorated with Ag_5Au_5 and Ag_9Pt clusters. The aim of these calculations is to support experiment and explain the observed enhanced sensitivity and the change in selectivity reported for the systems studied.

Terminations A and B of the ZnO(10$\bar{1}$0) surface were modelled using slabs with an area of 98.574 Å^2 and containing 96 atoms distributed in 8 atomic layers, see Fig. 7a. A vacuum gap of 20 Å along the direction perpendicular to the surface was added to separate each slab from its periodic image. More details regarding the stacking of the layers, and a description of the surface terminations and the number of layers with the atoms frozen at their bulk positions can be found elsewhere.[49]

The substitutional doping of the ZnO(10$\bar{1}$0) surface by Ag and its effect on the surface structure, energies, as well as on the electronic and magnetic properties are now examined. One Zn atom is replaced, in order to model the lowest Ag content value of 2.73 wt%, which is allowed by the size of our 48 formula unit (f.u.) computational cell. Despite modelling a dopant concentration almost threefold higher than the 0.95 wt% used for the experiments, previous works have shown excellent agreement between the two approaches.[32,49] The substitutional doping of the symmetrically inequivalent exposed Zn atoms was inspected, corresponding to the following solid-state reaction,

$$Zn_{48}O_{48}(10\bar{1}0) + Ag(fcc) = Zn_{47}AgO_{48}(10\bar{1}0) + Zn(hcp) \quad (8)$$

where the face-centred cubic (fcc) Ag and hexagonal close packed (hcp) Zn were modelled using the one and two atoms primitive unit cells, respectively.

The surface free energy (σ) of the partially decorated material has been estimated using,

$$\sigma = \gamma_r + \frac{E_{dop} - E_{pris} - E_{Ag} + E_{Zn}}{A} \quad (9)$$

where γ_r is the surface energy for the relaxed pristine ZnO(10$\bar{1}$0) surface, E_{dop} is the energy of the Ag-doped ZnO(10$\bar{1}$0) surface, E_{pris} is the energy of the pristine ZnO(10$\bar{1}$0) surface, E_{Ag} is the energy of one atom in the bulk of fcc Ag and E_{Zn} is the energy of one atom in the bulk of hcp Zn. The γ_r values for the relaxed pristine ZnO(10$\bar{1}$0) surface were taken from previous work,[12] and Table S2† shows the experimental and simulated lattice parameters for Ag and Zn.

Table 3 displays the surface free energies for the Ag-doped systems, indicating that only termination A is slightly stabilised by 14–18 meV Å^{-2} with respect to its pristine parent structure. However, substitutional doping of termination B, and in particular of its 3-fold Zn site, lead to the most thermodynamically stable doped surfaces, although they are less favourable than the pristine parent plane. The simulations suggest that in both terminations, doping the most exposed undercoordinated cation positions is ~5 meV Å^{-2} more favourable than the substitution of the 4-fold sites. It was found that large in-plane displacements of approximately 1 Å for the atoms within the topmost layer account for the exothermic enthalpy during the insertion of Ag in termination A. Moreover, minor concomitant shifts of 0.15 Å towards the bulk are also observed for the sub-surface plane of Zn atoms and the surface layer of counter-anions. These horizontal and vertical atomic shifts are only allowed in the doped termination A due to the large interlayer spacing of 1.848 Å between the surface and sub-surface planes.[49] In contrast, the densest topmost layers of termination B experience negligible displacements, with the exception of the O atoms surrounding the 3- and 4-fold Ag dopants, which move by 0.43 and 0.15 Å, respectively.

Bader charge analysis[78–80] shows that Zn ions draw 58–60% of the electrons required to become neutral atoms from the Ag atoms, in agreement with their different charges in the pristine and doped surfaces, respectively. However, the largest electronic transfer is 68% when the 3-fold position of termination B is doped, which is also the most stable surface of this study. We found different redox compensation mechanisms for the electronic deficit caused by the replacement of the Zn atoms in the two terminations of the ZnO(10$\bar{1}$0) surface. In termination A, the 3-fold Zn ions provide an excess of electrons, which also reduces the exposed oxygen atoms by a further 0.1e, thereby increasing the ionic character of the topmost surface layer. In termination B, the scenario for the charge compensation of Zn only involves the oxidation of its neighbouring oxygen atoms as illustrated in Fig. 7b. The charge density difference schemes were constructed by subtracting the sum of the electron charge densities of the clean surface and isolated dopant, with identical structure as in the doped form, from the electron density of the total system obtained from static calculations. The

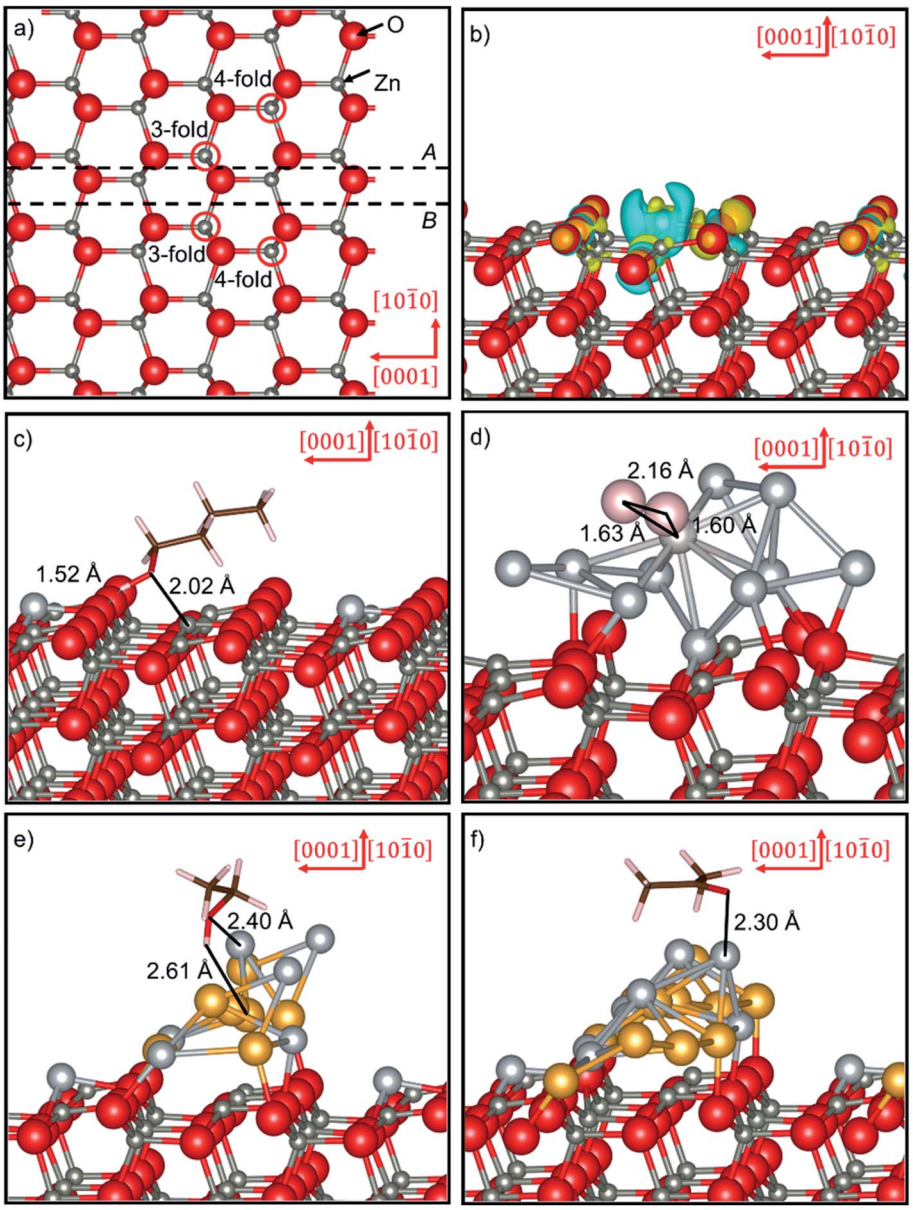

Fig. 7 (a) Side view of the simulation slabs for terminations A and B of the ZnO(10$\bar{1}$0) surface. The 3- and 4-fold Zn positions that were doped with Ag are displayed within red circles, and the dashed lines represent the surface terminations. (b) Charge density flow (ρ) for the substitutional doping of the 3-fold Zn positions in termination B of the ZnO(10$\bar{1}$0) surface. Electron density gain and depletion surfaces are in yellow and green, respectively. Isosurfaces display a value of ± 0.002 e Å^{-3}. (c) Molecular adsorption of n-C_4H_9OH on the termination B of the ZnO(10$\bar{1}$0):Ag surface. (d) Dissociative adsorption of H_2 on the termination B of the Ag_9Pt/ZnO(10$\bar{1}$0):Ag surface. (e) Molecular adsorption of C_2H_5OH and (f) CH_3COCH_3 on the termination B of the Ag_uAu_5/ZnO(10$\bar{1}$0):Ag surface. Crystallographic directions are indicated for all panels.

simulation of the doped terminations A and B suggests that most atoms remain non-magnetic following the process represented in eqn (8). However, the Ag introduced, alongside the 3-fold oxygen ions that directly coordinate it, become slightly magnetic at *ca.* 0.3 μ_B per atom. From the small magnetic moment calculated for the dopant, an electronic distribution of $e^2_\uparrow e^2_\downarrow t^3_\uparrow t^3_\downarrow$ has been inferred, corresponding to Ag^+ ions in a pseudo-tetrahedral crystal field of oxygen atoms.

The electronic properties of the doped surfaces were further interrogated by measuring the work function (Φ) in order to gauge their reactivity as reducing agents.[32,49] The work function is the energy needed to remove an electron from the Fermi level (E_F) of the surface into the electrostatic potential of the vacuum (V_V), calculated as $\Phi = V_V - E_F$. Table 3 shows large reductions of over 50% in the work function values of all the doped surfaces with respect to their pristine counterparts. The absolute value for this type of thermodynamic work is between 2.61 and 2.64 eV for the doped 4-fold position in both terminations. However, for further analysis, we focus on the 3-fold doped slab of termination B, which possesses the lowest surface energy and is therefore likely to be the prominent plane exposed in the crystal morphology of ZnO.

Table 3 Calculated surface energies after relaxation (γ_r) for terminations A and B of the pristine ZnO(10$\bar{1}$0) surface.[49] The surface free energies (σ) are also reported for both terminations of the Ag-doped ZnO(10$\bar{1}$0) surface. The work function (Φ) values are indicated for the pristine[49] and doped surfaces

Termination	Doping site	γ_r/σ (meV Å^{-2})	Φ (eV)
A	Pristine	190	5.40
	3-Fold	172	2.50
	4-Fold	176	2.61
B	Pristine	84	5.80
	3-Fold	125	2.84
	4-Fold	130	2.64

Impregnation with Ag_5Au_5 and Ag_9Pt was also explored as a means to tune the sensing properties of the doped ZnO(10$\bar{1}$0) surface and to reduce the detection limit of VOCs. Clusters composed of 10 atoms were chosen, as this is the smallest size to produce a close analogue to the experimental Ag content, *i.e.* 48 at% and 88 at% in AgAu and AgPt NPs, respectively (*cf.* Table S1†). The initial geometries for both noble bimetallic nanoclusters were derived from the fcc crystal structure common to the three monometallic materials[81–83] and the secondary Au or Pt element was placed at random crystallographic positions. Table S2† illustrates the excellent agreement between the experimental and simulated lattice parameters for monometallic Au and Pt. Three different positions for the adsorption of the bimetallic clusters were tested, *i.e.* (i) above, (ii) close to, and (iii) far away from the Ag dopant. The term $-(xE_{Ag} + yE_X)/A$ was added to eqn (9), to evaluate the surface free energy of the fully decorated material; where X represents either fcc Au or Pt; E_X is the energy of one such atom in the bulk; x and y are the numbers of Ag and X atoms, respectively, in the cluster; E_{dop} becomes $E_{dop+clus}$, which is the energy of the Ag-doped ZnO(10$\bar{1}$0) surface decorated with the NPs; while the remaining variables keep their previous definition. The simulations suggest that the addition of the bimetallic clusters increases the surface free energy with respect to the doped surface, particularly for the Pt-based particles, see Table 4. The most thermodynamically favourable adsorption position depends on the nature of the cluster, as Ag_5Au_5 is likely to sit far from the Ag dopant, while Ag_9Pt prefers a closer position.

Table 4 Calculated surface free energy (σ) and work function (Φ) for the Ag-doped ZnO(10$\bar{1}$0) surface decorated with the Ag_5Au_5 and Ag_9Pt clusters. The adsorption energy (E_{ads}) for the NPs on the Ag-doped ZnO(10$\bar{1}$0) surface is reported. The relative position of the NP with respect to the Ag-dopant is also indicated. The doping was carried out in the 3-fold position of termination B

Cluster	Position	σ (meV Å^{-2})	E_{ads} (eV)	Φ (eV)
Ag_5Au_5	Above	181	5.54	3.01
	Close	184	5.88	3.10
	Far	179	5.32	3.12
Ag_9Pt	Above	192	6.63	2.95
	Close	209	8.30	2.95
	Far	194	6.79	3.15

The stability of the clusters on the surface was calculated using the adsorption energy (E_{ads}):

$$E_{ads} = E_{dop+clus} - E_{dop} - xE_{Ag} - yE_X \quad (10)$$

whose calculated values are in agreement with the trend in surface free energies for the Ag_5Au_5 clusters only, see Table 4. The lack of correlation between the adsorption energies of Ag_9Pt and their surface free energies can be explained based on the random position that Pt can adopt within the cluster during geometry optimisation. The positive values calculated for all the adsorption energies, which are largest for Ag_5Au_5, indicate that although these are thermodynamically unfavourable processes, the impregnated clusters are stable due to strong cohesive forces. Interestingly, the lowest adsorption energy values of 5.32 and 2.95 eV were calculated for the most stable adsorption position of the Au- and Pt-based NPs, respectively.

The incorporation of both nanoclusters slightly raises the work function of the fully decorated surfaces with respect to the doped system. The lowest work function is predicted for the facet containing the Ag_9Pt NP in the most favourable adsorption position. However, the largest value for this type of thermodynamic work was calculated for the surface decorated using the Ag_5Au_5 cluster in the most stable binding site. The small magnetic moments of the Ag dopant vanish after adsorption of the nanoclusters in any of the positions considered. Most of the adsorbed clusters are non-magnetic, but the simulations reveal a small mean value of 0.04 μ_B for each atom within the Ag_5Au_5 particles sited above and close to the dopant. Large positive charges of $1.4e^-$ are located on the Ag atom of the cluster, while the secondary Au and Pt metals are reduced by -0.7 and $-0.4e^-$, in agreement with their respective electronegativities. Upon adsorption, the net charge balance results in all noble bimetallic particles losing $\sim 0.9e^-$ to the Zn atoms underneath and the O ions near the dopant.

The adsorption of the single molecules onto the doped and NP decorated ZnO(10$\bar{1}$0) surfaces was also studied and it was found that all these processes release energy, see Table 5. The molecules were introduced in several orientations at 1.5 Å from the surface and were subsequently allowed to relax to their equilibrium adsorption geometries. The calculated adsorption energies on the Ag-doped surface are roughly -1.5 to -1.7 eV for all the alcohols, which subtly depends directly on their molar mass. However, the strength of binding is approximately 0.5 eV less favourable for CH_3COCH_3 than for the alcohols, owing to the different chemical nature of their carbonyl and hydroxyl functional groups. The simulations suggest that the non-polar H_2 molecule has the overall lowest adsorption energy at ~ -1.0 eV. The introduction of the Ag_9Pt nanocluster reduces the energetic preference of the alcohols and ketone for the decorated surface by approximately 1.0 and 0.5 eV, respectively, compared to the doped system. The largest energy released at $E_{ads} = -1.387$ eV was found for the adsorption of H_2 on the Ag_9Pt/ZnO:Ag surface, indicating a change in selectivity in agreement with our experiments. The impregnation with

Table 5 Adsorption energies (E_{ads}) and charge transfers (Δq) for the CH_3CH_2OH, CH_3COCH_3, n-C_4H_9OH, 2-C_3H_7OH, CH_3OH and H_2 molecules on the Ag-doped ZnO(10$\bar{1}$0) surface and following decoration with the Ag_5Au_5 and Ag_9Pt clusters. The relative position of the adsorbate with respect to the dopant is also indicated. The doping was carried out in the 3-fold position of termination B. Negative values of Δq indicate a charge transfer from the surface to the adsorbate

		ZnO(10$\bar{1}$0):Ag		Ag_9Pt		Ag_5Au_5	
Molecule	Position	E_{ads} (eV)	Δq (e^-)	E_{ads} (eV)	Δq (e^-)	E_{ads} (eV)	Δq (e^-)
CH_3CH_2OH	Defect	−1.527	0.09	−0.590	−0.04	−0.762	0.00
	Close	−1.486	0.02				
	Far	−1.602	0.03				
CH_3COCH_3	Defect	−1.122	0.07	−0.663	0.02	−0.798	0.00
	Close	−1.021	0.04				
	Far	−1.027	0.04				
n-C_4H_9OH	Defect	−1.485	0.08	−0.545	0.04	−0.551	−0.02
	Close	−1.632	0.03				
	Far	−1.706	0.03				
2-C_3H_7OH	Defect	−1.616	0.09	−0.555	0.05	−0.798	0.00
	Close	−1.530	0.03				
	Far	−1.597	0.03				
CH_3OH	Defect	−1.469	0.08	−0.453	−0.07	−0.528	−0.02
	Close	−1.425	0.02				
	Far	−1.456	0.02				
H_2	Defect	−1.046	0.44	−1.387	−0.07	−0.070	−0.02
	Close	−0.268	0.02				
	Far	−0.291	0.03				

Ag_5Au_5 NPs leads to larger adsorption energies and enhanced sensitivity towards the VOCs with respect to the Ag_9Pt/ZnO:Ag surface. Remarkably, the decreasing order of binding strength for the organic molecules is $E_{ads}(CH_3COCH_3) \approx E_{ads}(2\text{-}C_3H_7OH) \approx E_{ads}(C_2H_5OH) > E_{ads}(n\text{-}C_4H_9OH) \approx E_{ads}(CH_3OH)$, showing no dependence on the type of functional group. The binding energy of −0.070 eV for H_2 on Ag_5Au_5/ZnO:Ag is the lowest calculated in this study, which explains the lack of selectivity found in our experiments for this molecule.

All the VOCs adsorb molecularly on the doped as well as on the NP-decorated ZnO(10$\bar{1}$0) surfaces, in line with previous reports.[32,49] On the doped surface, three adsorption positions relative to the Ag atom were tested, *i.e.* the molecules directly interacting with the defect, or with its first or second nearest Zn neighbours. In the case of the VOCs, the preferred mode involves direct coordination between the adsorbate oxygen and the exposed Ag or Zn atom at around 2.15 and 2.00 Å, respectively. The hydroxy group of the alcohols forms a short hydrogen-bond at a distance of 1.39 to 1.53 Å with a surface 3-fold oxygen atom, as shown in Fig. 7c for n-C_4H_9OH. Other configurations are at least 0.108 eV less favourable than the most stable binding modes, as they involve dissociative adsorption or distorted hydrogen-bonds. For example, CH_3OH can dissociate the hydroxy hydrogen, which is donated to the closest oxygen from the coordinated Ag adsorption site. Moreover, n-C_4H_9OH can form hydrogen-bonds with the oxygens lying either closer or farther away from the coordinated Ag and Zn cation than in the most stable adsorption modes. The free rotation around the C–OH bond and weak dispersion forces allow the hydrocarbon fragment of the alcohols to orientate as close as possible to the surface in all the adsorption modes. In contrast, the flat ketone molecule stays adsorbed in a canted configuration, owing to the tetrahedral nature of the metallic coordination site and the trigonal geometry of the sp^2-hybridised carbonyl oxygen. Unsurprisingly, the H_2 molecule has both minor exothermic molecular and moderately exothermic dissociative adsorption modes. This molecule appears tilted and hovering at 2.10 Å from any of the Zn sites and the closest 3-fold oxygen. H_2 also dissociates upon interaction with the AgO or OO pair sites. For the dissociative adsorption configurations, the hydrogen atoms sit at 1.63 Å from the Ag-dopant and at the usual O–H bond distance of 0.98 Å from the 3-fold oxygen.

The addition of Ag_9Pt changes the adsorption geometry of CH_3OH, which prefers to interact through its hydroxy H with the Pt at a distance of 2.30 Å, which increases by 0.38 Å for C_2H_5OH. However, the alcohols of higher molar mass, *i.e.* n-C_4H_9OH and 2-C_3H_7OH, instead coordinate to the Pt atom by their hydroxy O at an average distance of 2.37 Å. CH_3COCH_3 binds the Pt atom at 2.20 Å, which is the smallest value reported for any VOC interacting with the Ag_9Pt/ZnO:Ag surface. Different behaviours were calculated for the hydrocarbon radical of the VOCs, which lies more parallel to the surface for the low mass alcohols and the ketone than for n-C_4H_9OH and 2-C_3H_7OH. H_2 dissociates upon adsorption to the Pt site, with the H atoms separated by 2.16 Å, explaining the largest exothermic enthalpy for the interaction with the supported Ag_9Pt cluster, as shown in Fig. 7d. Shifting to the Ag_5Au_5 particle increases the number of interactions between the surface and the VOC molecules, justifying the larger adsorption energies with respect to the Ag_9Pt/ZnO:Ag surface. The DFT adsorption geometries indicate that 2-C_3H_7OH and C_2H_5OH form the dative O–Ag and H–Au bonds at 2.40 and 2.62 Å, respectively, see Fig. 7e. Furthermore, n-C_4H_9OH and CH_3OH have similar adsorption configurations as the alcohols of intermediate molecular mass, but coordinate

the Au atom at least 0.14 Å further away. CH_3COCH_3 can only form the O–Ag interaction at 2.30 Å, which is the shortest for the bimetallic Ag_5Au_5 cluster, as displayed in Fig. 7f. Finally, the H_2 molecule stays perpendicular to the surface and 2.92 Å from the Au atom, leading to the smallest adsorption energy calculated for this molecule in this study.

Bader charge analysis shows that all VOCs become positively charged upon adsorption on the doped surface, with the largest transfer of $0.09e^-$ obtained for the Ag site, as shown in Table 5. Charge donations decrease around 50% after introducing the Ag_9Pt cluster and the negative values calculated for the low molecular mass alcohols confirm their adsorption geometry *via* the hydroxy H. Electron transfers vanish for the molecules adsorbed on Ag_5Au_5, with the exception of the negatively charged *n*-C_4H_9OH and CH_3OH, which sit furthest away from the cluster. H_2 suffers the largest charge withdrawal reported for adsorptions on the doped surface but it is predicted that the H–Zn hydrogen gains $-0.20e^-$ while the hydroxy H loses $0.64e^-$. The reverse direction of electron transport for the interaction with the bimetallic nanoclusters was observed, as H_2 gains small electronic charge and remains molecular.

We believe that the change in selectivity is the result of adding Pt, which displays excellent catalytic properties for binding and dissociating the H_2 molecule, which was discussed in the section "Gas sensing mechanism for bimetallic alloy NP-decorated films". The computational simulations that we performed provide further insight into the sensing mechanism at the molecular level. We have studied the adsorption of VOCs and H_2 onto the surfaces of the pristine ZnO($10\bar{1}0$):Ag surface and after impregnation of the alloy nanoparticles. Upon adsorption, the VOCs release the largest adsorption energies on the pristine ZnO($10\bar{1}0$):Ag facet. The pristine surface contains the largest proportion of positively charged Zn cations exposed, which are available to coordinate the O atoms of the VOCs. As a result, the H_2 and VOC molecules donate charge to the surface and become positively charged, see Table 5. However, the introduction of the clusters reduces the number of accessible surface Zn atoms, decreasing considerably the adsorption energy and charge transfers of the VOCs, which in many cases experience a net electron gain. In particular, the Pt atom of the Ag_9Pt nanoparticle is able to dissociate catalytically the H_2 molecule, which displays the largest adsorption energy in comparison to the VOCs. For the surfaces decorated with the Ag_5Au_5 NPS, we calculated the largest difference of adsorption energy between VOCs and H_2 molecule. This enhanced sensitivity compared to the pristine surface can be rationalized in terms of the number of interactions that the VOC molecules are able form with the Au atoms in the Ag_5Au_5 clusters. Thus, the computational results are in agreement, complement and explain the changes in selectivity and sensitivity observed experimentally.

Conclusions

In summary, the surface of ZnO:Ag nanostructured columnar grains was successfully decorated with AgPt and AgAu bimetallic noble bimetallic alloy NPs using a custom-made high vacuum deposition system with an in-house Haberland type gas aggregation source. Gas sensing measurements were carried out to reveal the response of the thin films to H_2 gas and various VOC vapors. The underlying gas sensing mechanisms for the AgPt as well as AgAu NP-decorated ZnO:Ag thin films was proposed and discussed in terms of the electronic and chemical sensitization effect of the bimetallic alloy NPs.

The nanocomposites with AgAu NPs exhibit a highly improved response to VOC vapors compared to the pristine ZnO:Ag thin films and previously reported nanocomposites based on ZnO:Ag and Ag NPs. The gas response to 100 ppm of ethanol, acetone, *n*-butanol, 2-propanol and methanol vapors was increased by a factor of ~2.8, ~6, ~3.2, ~3 and ~4.5, respectively, compared to pristine ZnO:Ag thin films. In contrast, the nanocomposite decorated with the AgPt NPs shows a remarkable change in selectivity to H_2 gas. While the response to all VOC vapors is considerably decreased once AgPt NPs are introduced on the surface of ZnO:Ag columnar films, the response toward H_2 is increased by more than one order of magnitude.

The affinity of small molecules towards the doped and NP decorated ZnO($10\bar{1}0$) surfaces was also investigated computationally. Doping with Ag atoms was modelled, where it was found that the most stable substitution occurs for the 3-fold Zn surface sites. Subsequently, Ag_9Pt and Ag_5Au_5 clusters prefer to bind the surface above and far away from the dopant atom, respectively. When studying the binding of CH_3CH_2OH, CH_3COCH_3, *n*-C_4H_9OH, 2-C_3H_7OH, CH_3OH and H_2 on the doped surfaces and at the nanoclusters, it was found that the VOCs release the largest and smallest energies upon adsorption to the doped surfaces and Ag_9Pt cluster, respectively, in agreement with the enhanced selectivity of the former. The dissociative adsorption of H_2 on the Ag_9Pt/ZnO($10\bar{1}0$):Ag surface causes the largest calculated adsorption energy for any of the NP-decorated surfaces, supporting the change in selectivity reported for this system.

We have shown that the decoration of ZnO:Ag columnar thin films with noble bimetallic NPs provides a viable route to tailor the sensitivity as well as selectivity of ZnO:Ag gas sensors. It was found that AgAu NPs lead to high sensitivity as well as fast response and recovery times for the detection of the VOC types studied. In addition, the possibility to change the selectivity of ZnO:Ag thin films by surface decoration with bimetallic NPs is a feasible, effective and flexible approach for the fabrication of highly selective sensors.

Considering the low concentration of about 12 at% of Pt in the AgPt bimetallic alloy NPs, this sensor is a promising prototype of a cost effective H_2 gas sensor for early hazard detection in lithium ion batteries. Given the high versatility and adaptability of the thin film fabrication process, in combination with the application of alloy NPs for surface decoration, the approach presented in this work offers significant potential for gas sensing applications, for example for the early detection of thermal runaway in lithium ion batteries LIB.

Author contributions

A. V., V. P., and O. L. synthesized the ZnO:Ag nanomaterial functionalized using AgAu and AgPt bimetallic alloy NPs. O. L.

developed the synthesis methodology from chemical solution (SCS) for ZnO. A. V. and F. F. developed the functionalization procedure for the AgAu and AgPt bimetallic alloy NPs, and set-up all experiments and XPS analysis. O. L., V. P., A. V., M. I. T., M. H., H. C. and S. N. adapted a technological approach for material synthesis and integration/fabrication of the sensors for early hazard detection in batteries. V. P. and O. L. carried out the measurement of the sensing properties of the thin film materials and analyzed the data. T. D., N. W. and L. K. performed the TEM studies and analysis. V. P., O. L., S. N., R. A., M. I. T. and H. C. analyzed the results, including the experimental data and the revised draft. N. H. d. L., D. S. C. and A. C. E. realized the computational part and revised draft. D. S. C. analysed the computational results. A. V., P. V., D. S. C., S. N., T. D., N. W. and O. L. prepared the manuscript draft. O. L., A. V., F. F., L. K., S. N. and R. A. conducted the study conception and design, and gave the final approval of the manuscript version to be published. The manuscript was written through contributions of all authors. All authors reviewed the manuscript. Katrin Brandenburg is acknowledged for her help in the final proof-reading of the manuscript.

Data availability

All data created during this research is openly available from Cardiff University's Research Portal at http://www.doi.org/10.17035/d.2019.0081500252.

Conflicts of interest

There are no conflicts to declare.

Acknowledgements

Dr Lupan acknowledges the Alexander von Humboldt Foundation for the research fellowship for experienced researchers 3-3MOL/1148833 STP at the Institute for Materials Science, Kiel University, Germany. This research was funded partially by the German Research Foundation (DFG) under schemes SFB1261 and FOR2093 'Memristive devices for neuronal systems' as well as by the Federal Ministry of Education and Research in Germany under project "PorSSi" (03XP0126 B). Dr O. Polonskyi is acknowledged for fruitful discussions of XPS part. This research was sponsored in part by the NATO Science for Peace and Security Programme (SPS) under grant G5634 "Advanced Electro-Optical Chemical Sensors" AMOXES. N. H. d. L., D. S. C. and A. C. E. acknowledge the Engineering and Physical Sciences Research Council (EPSRC grant EP/K009567/2) for funding. *Via* their membership of the UK's HEC Materials Chemistry Consortium, which is funded by EPSRC (EP/L000202/1, EP/R029431/1), this work used the ARCHER UK National Supercomputing Service (https://www.archer.ac.uk). This work also employed the computational facilities of the Advanced Research Computing @ Cardiff (ARCCA) Division, Cardiff University and the Supercomputing Facilities at Cardiff University operated by ARCCA on behalf of the Cardiff Supercomputing Facility and the Supercomputing Wales (SCW) projects. We acknowledge the support of the latter, which is part-funded by the European Regional Development Fund (ERDF) *via* Welsh Government. The authors thank Salih Veziroglu for his contribution to the design and the graphic illustration of the cover graphic.

References

1 O. Lupan, V. Postica, F. Labat, I. Ciofini, T. Pauporté and R. Adelung, Ultra-Sensitive and Selective Hydrogen Nanosensor With Fast Response at Room Temperature Based on a Single Pd/ZnO Nanowire, *Sens. Actuators, B*, 2018, **254**, 1259–1270.

2 A. Kolmakov, D. O. Klenov, Y. Lilach, S. Stemmer and M. Moskovits, Enhanced Gas Sensing by Individual SnO_2 Nanowires and Nanobelts Functionalized with Pd Catalyst Particles, *Nano Lett.*, 2005, **5**, 667–673.

3 N. Yamazoe, New approaches for improving semiconductor gas sensors, *Sens. Actuators, B*, 1991, **5**, 7–19.

4 S. Bano, N. Ahmad, S. Sultana, S. Sabir and M. Z. Khan, Preparation and study of ternary polypyrrole-tin oxide-chitin nanocomposites and their potential applications in visible light photocatalysis and sensors, *J. Environ. Chem. Eng.*, 2019, **7**, 103012.

5 H. Tian, H. Fan, J. Ma, Z. Liu, L. Ma, S. Lei, J. Fang and C. Long, Pt-decorated zinc oxide nanorod arrays with graphitic carbon nitride nanosheets for highly efficient dual-functional gas sensing, *J. Hazard. Mater.*, 2018, **341**, 102–111.

6 L. Ma, H. Fan, H. Tian, J. Fang and X. Qian, The n-ZnO/n-In_2O_3 heterojunction formed by a surface-modification and their potential barrier-control in methanal gas sensing, *Sens. Actuators, B*, 2016, **222**, 508–516.

7 J. Li, H. Fan and X. Jia, Multilayered ZnO Nanosheets with 3D Porous Architectures: Synthesis and Gas Sensing Application, *J. Phys. Chem. C*, 2010, **114**, 14684–14691.

8 H. Tian, H. Fan, J. Ma, L. Ma and G. Dong, Noble metal-free modified electrode of exfoliated graphitic carbon nitride/ZnO nanosheets for highly efficient hydrogen peroxide sensing, *Electrochim. Acta*, 2017, **247**, 787–794.

9 S.-S. Chen, X.-X. Lin, A.-J. Wang, H. Huang and J.-J. Feng, Facile synthesis of multi-branched AgPt alloyed nanoflowers and their excellent applications in surface enhanced Raman scattering, *Sens. Actuators, B*, 2017, **248**, 214–222.

10 O. Lupan, V. Postica, R. Adelung, F. Labat, I. Ciofini, U. Schürmann, L. Kienle, L. Chow, B. Viana and T. Pauporté, Functionalized Pd/ZnO Nanowires for Nanosensors, *Phys. Status Solidi RRL*, 2017, **12**, 1700321.

11 J. Guo, J. Zhang, M. Zhu, D. Ju, H. Xu and B. Cao, High-performance gas sensor based on ZnO nanowires functionalized by Au nanoparticles, *Sens. Actuators, B*, 2014, **199**, 339–345.

12 S. M. Majhi, P. Rai and Y.-T. Yu, Facile Approach to Synthesize Au@ZnO Core–Shell Nanoparticles and Their Application for Highly Sensitive and Selective Gas Sensors, *ACS Appl. Mater. Interfaces*, 2015, **7**, 9462–9468.

13 O. Lupan, V. Postica, N. Wolff, J. Su, F. Labat, I. Ciofini, H. Cavers, R. Adelung, O. Polonskyi, F. Faupel, L. Kienle, B. Viana and T. Pauporté, Low-Temperature Solution Synthesis of Au-Modified ZnO Nanowires for Highly Efficient Hydrogen Nanosensors, *ACS Appl. Mater. Interfaces*, 2019, **11**, 32115–32126.

14 A. Shafi, N. Ahmad, S. Sultana, S. Sabir and M. Z. Khan, Ag_2S-Sensitized NiO–ZnO Heterostructures with Enhanced Visible Light Photocatalytic Activity and Acetone Sensing Property, *ACS Omega*, 2019, **4**, 12905–12918.

15 J. P. V. Damasceno, C. M. Maroneze, M. Strauss, F. A. Sigoli and I. O. Mazali, Preparation of supported AuPd nanoalloys mediated by ionic liquid-like functionalized SBA-15: structural correlations concerning its catalytic activity, *New J. Chem.*, 2016, **40**, 6636–6642.

16 Y. Yong, C. Li, X. Li, T. Li, H. Cui and S. Lv, Ag_7Au_6 Cluster as a Potential Gas Sensor for CO, HCN, and NO Detection, *J. Phys. Chem. C*, 2015, **119**, 7534–7540.

17 S.-J. Kim, S.-J. Choi, J.-S. Jang, H.-J. Cho, W.-T. Koo, H. L. Tuller and I.-D. Kim, Exceptional High-Performance of Pt-Based Bimetallic Catalysts for Exclusive Detection of Exhaled Biomarkers, *Adv. Mater.*, 2017, **29**, 1700737.

18 M. M. Rahman, S. B. Khan, A. M. Asiri, K. A. Alamry, A. A. P. Khan, A. Khan, M. A. Rub and N. Azum, Acetone sensor based on solvothermally prepared ZnO doped with Co_3O_4 nanorods, *Microchim. Acta*, 2013, **180**, 675–685.

19 S.-W. Choi, A. Katoch, G.-J. Sun and S. S. Kim, Bimetallic Pd/Pt nanoparticle-functionalized SnO_2 nanowires for fast response and recovery to NO_2, *Sens. Actuators, B*, 2013, **181**, 446–453.

20 F. Fan, J. Zhang, J. Li, N. Zhang, R. Hong, X. Deng, P. Tang and D. Li, Hydrogen sensing properties of Pt-Au bimetallic nanoparticles loaded on ZnO nanorods, *Sens. Actuators, B*, 2017, **241**, 895–903.

21 K. Hassan and G.-S. Chung, Catalytically activated quantum-size Pt/Pd bimetallic core–shell nanoparticles decorated on ZnO nanorod clusters for accelerated hydrogen gas detection, *Sens. Actuators, B*, 2017, **239**, 824–833.

22 T. Shiravand and A. Azadbakht, Impedimetric biosensor based on bimetallic AgPt nanoparticle-decorated carbon nanotubes as highly conductive film surface, *J. Solid State Electrochem.*, 2017, **21**, 1699–1711.

23 K. K. Haldar, S. Kundu and A. Patra, Core-Size-Dependent Catalytic Properties of Bimetallic Au/Ag Core–Shell Nanoparticles, *ACS Appl. Mater. Interfaces*, 2014, **6**, 21946–21953.

24 Z. Y. Li, J. P. Wilcoxon, F. Yin, Y. Chen, R. E. Palmer and R. L. Johnston, Structures and optical properties of 4-5 nm bimetallic AgAu nanoparticles, *Faraday Discuss.*, 2008, **138**, 363–373.

25 M. Metzger, B. Strehle, S. Solchenbach and H. A. Gasteiger, Origin of H_2 Evolution in LIBs: H_2O Reduction vs. Electrolyte Oxidation, *J. Electrochem. Soc.*, 2016, **163**, A798–A809.

26 D. Ortiz, V. Steinmetz, D. Durand, S. Legand, V. Dauvois, P. Maître and S. Le Caër, Radiolysis as a solution for accelerated ageing studies of electrolytes in lithium-ion batteries, *Nat. Commun.*, 2015, **6**, 6950.

27 A. W. Golubkov, D. Fuchs, J. Wagner, H. Wiltsche, C. Stangl, G. Fauler, G. Voitic, A. Thaler and V. Hacker, Thermal-runaway experiments on consumer Li-ion batteries with metal-oxide and olivin-type cathodes, *RSC Adv.*, 2014, **4**, 3633–3642.

28 V. Postica, I. Hölken, V. Schneider, V. Kaidas, O. Polonskyi, V. Cretu, I. Tiginyanu, F. Faupel, R. Adelung and O. Lupan, Multifunctional device based on ZnO:Fe nanostructured films with enhanced UV and ultra-fast ethanol vapour sensing, *Mater. Sci. Semicond. Process.*, 2016, **49**, 20–33.

29 J. Gröttrup, V. Postica, N. Ababii, O. Lupan, C. Zamponi, D. Meyners, Y. K. Mishra, V. Sontea, I. Tiginyanu and R. Adelung, Size-Dependent UV and Gas Sensing Response of Individual Fe_2O_3-ZnO:Fe Micro- and Nanowire Based Devices, *J. Alloys Compd.*, 2017, **701**, 920–925.

30 O. Lupan, L. Chow, S. Shishiyanu, E. Monaico, T. Shishiyanu, V. Ṣontea, B. Roldan Cuenya, A. Naitabdi, S. Park and A. Schulte, Nanostructured zinc oxide films synthesized by successive chemical solution deposition for gas sensor applications, *Mater. Res. Bull.*, 2009, **44**, 63–69.

31 O. Lupan, S. Shishiyanu, V. Ursaki, H. Khallaf, L. Chow, T. Shishiyanu, V. Sontea, E. Monaico and S. Railean, Synthesis of nanostructured Al-doped zinc oxide films on Si for solar cells applications, *Sol. Energy Mater. Sol. Cells*, 2009, **93**, 1417–1422.

32 V. Postica, A. Vahl, D. Santos-Carballal, T. Dankwort, L. Kienle, M. Hoppe, A. Cadi-Essadek, N. H. de Leeuw, M.-I. Terasa, R. Adelung, F. Faupel and O. Lupan, Tuning ZnO Sensors Reactivity toward Volatile Organic Compounds via Ag Doping and Nanoparticle Functionalization, *ACS Appl. Mater. Interfaces*, 2019, **11**, 31452–31466.

33 O. Polonskyi, T. Peter, A. M. Ahadi, A. Hinz, T. Strunskus, V. Zaporojtchenko, H. Biederman and F. Faupel, Huge increase in gas phase nanoparticle generation by pulsed direct current sputtering in a reactive gas admixture, *Appl. Phys. Lett.*, 2013, **103**, 033118.

34 H. Haberland, M. Karrais, M. Mall and Y. Thurner, Thin films from energetic cluster impact: a feasibility study, *J. Vac. Sci. Technol., A*, 1992, **10**, 3266–3271.

35 P. Solař, O. Polonskyi, A. Olbricht, A. Hinz, A. Shelemin, O. Kylián, A. Choukourov, F. Faupel and H. Biederman, Single-step generation of metal-plasma polymer multicore@shell nanoparticles from the gas phase, *Sci. Rep.*, 2017, **7**, 8514.

36 A. Vahl, J. Strobel, W. Reichstein, O. Polonskyi, T. Strunskus, L. Kienle and F. Faupel, Single target sputter deposition of alloy nanoparticles with adjustable composition via a gas aggregation cluster source, *Nanotechnology*, 2017, **28**, 175703.

37 O. Lupan, V. Postica, M. Mecklenburg, K. Schulte, Y. K. Mishra, B. Fiedler and R. Adelung, Low powered, tunable and ultra-light aerographite sensor for climate relevant gas monitoring, *J. Mater. Chem. A*, 2016, **4**, 16723–16730.

38 O. Lupan, V. Cretu, V. Postica, N. Ababii, O. Polonskyi, V. Kaidas, F. Schütt, Y. K. Mishra, E. Monaico, I. Tiginyanu, V. Sontea, T. Strunskus, F. Faupel and R. Adelung, Enhanced ethanol vapour sensing performances of copper oxide nanocrystals with mixed phases, *Sens. Actuators, B*, 2016, **224**, 434–448.

39 V. Cretu, V. Postica, A. K. Mishra, M. Hoppe, I. Tiginyanu, Y. K. Mishra, L. Chow, N. H. de Leeuw, R. Adelung and O. Lupan, Synthesis, characterization and DFT studies of zinc-doped copper oxide nanocrystals for gas sensing applications, *J. Mater. Chem. A*, 2016, **4**, 6527–6539.

40 G. Kresse and J. Hafner, Ab initio molecular dynamics for liquid metals, *Phys. Rev. B: Condens. Matter Mater. Phys.*, 1993, **47**, 558–561.

41 G. Kresse and J. Hafner, Ab initio molecular-dynamics simulation of the liquid-metal–amorphous-semiconductor transition in germanium, *Phys. Rev. B: Condens. Matter Mater. Phys.*, 1994, **49**, 14251–14269.

42 G. Kresse and J. Furthmüller, Efficient iterative schemes for ab initio total-energy calculations using a plane-wave basis set, *Phys. Rev. B: Condens. Matter Mater. Phys.*, 1996, **54**, 11169–11186.

43 G. Kresse and J. Furthmüller, Efficiency of ab-initio total energy calculations for metals and semiconductors using a plane-wave basis set, *Comput. Mater. Sci.*, 1996, **6**, 15–50.

44 P. E. Blöchl, Projector augmented-wave method, *Phys. Rev. B: Condens. Matter Mater. Phys.*, 1994, **50**, 17953–17979.

45 G. Kresse and D. Joubert, From ultrasoft pseudopotentials to the projector augmented-wave method, *Phys. Rev. B: Condens. Matter Mater. Phys.*, 1999, **59**, 1758–1775.

46 S. Grimme, J. Antony, S. Ehrlich and H. Krieg, A consistent and accurate ab initio parametrization of density functional dispersion correction (DFT-D) for the 94 elements H-Pu, *J. Chem. Phys.*, 2010, **132**, 154104.

47 S. Grimme, S. Ehrlich and L. Goerigk, Effect of the damping function in dispersion corrected density functional theory, *J. Comput. Chem.*, 2011, **32**, 1456–1465.

48 J. P. Perdew, K. Burke and M. Ernzerhof, Generalized Gradient Approximation Made Simple, *Phys. Rev. Lett.*, 1996, **77**, 3865–3868.

49 V. Postica, A. Vahl, J. Strobel, D. Santos-Carballal, O. Lupan, A. Cadi-Essadek, N. H. de Leeuw, F. Schütt, O. Polonskyi, T. Strunskus, M. Baum, L. Kienle, R. Adelung and F. Faupel, Tuning doping and surface functionalization of columnar oxide films for volatile organic compound sensing: experiments and theory, *J. Mater. Chem. A*, 2018, **6**, 23669–23682.

50 V. I. Anisimov, M. A. Korotin, J. Zaanen and O. K. Andersen, Spin bags, polarons, and impurity potentials in $La_{2-x}Sr_xCuO_4$ from first principles, *Phys. Rev. Lett.*, 1992, **68**, 345–348.

51 S. L. Dudarev, G. A. Botton, S. Y. Savrasov, C. J. Humphreys and A. P. Sutton, Electron-energy-loss spectra and the structural stability of nickel oxide: an LSDA+U study, *Phys. Rev. B: Condens. Matter Mater. Phys.*, 1998, **57**, 1505–1509.

52 D. O. Scanlon, B. J. Morgan and G. W. Watson, The origin of the enhanced oxygen storage capacity of $Ce_{1-x}(Pd/Pt)_xO_2$, *Phys. Chem. Chem. Phys.*, 2011, **13**, 4279–4284.

53 H. J. Monkhorst and J. D. Pack, Special points for Brillouin-zone integrations, *Phys. Rev. B: Solid State*, 1976, **13**, 5188–5192.

54 N. D. Mermin, Thermal Properties of the Inhomogeneous Electron Gas, *Phys. Rev.*, 1965, **137**, A1441–A1443.

55 H. Okamoto, Ag-Pt (silver-platinum), *J. Phase Equilib.*, 1997, **18**, 485.

56 G. L. W. Hart, L. J. Nelson, R. R. Vanfleet, B. J. Campbell, M. H. F. Sluiter, J. H. Neethling, E. J. Olivier, S. Allies, C. I. Lang, B. Meredig and C. Wolverton, Revisiting the revised Ag-Pt phase diagram, *Acta Mater.*, 2017, **124**, 325–332.

57 H. Tian, H. Fan, M. Li and L. Ma, Zeolitic Imidazolate Framework Coated ZnO Nanorods as Molecular Sieving to Improve Selectivity of Formaldehyde Gas Sensor, *ACS Sens.*, 2016, **1**, 243–250.

58 I.-S. Hwang, S.-J. Kim, J.-K. Choi, J.-J. Jung, D. J. Yoo, K.-Y. Dong, B.-K. Ju and J.-H. Lee, Large-scale fabrication of highly sensitive SnO_2 nanowire network gas sensors by single step vapor phase growth, *Sens. Actuators, B*, 2012, **165**, 97–103.

59 J. J. Hassan, M. A. Mahdi, C. W. Chin, H. Abu-Hassan and Z. Hassan, A high-sensitivity room-temperature hydrogen gas sensor based on oblique and vertical ZnO nanorod arrays, *Sens. Actuators, B*, 2013, **176**, 360–367.

60 A. Katoch, S.-W. Choi, H. W. Kim and S. S. Kim, Highly sensitive and selective H_2 sensing by ZnO nanofibers and the underlying sensing mechanism, *J. Hazard. Mater.*, 2015, **286**, 229–235.

61 A. Katoch, Z. U. Abideen, H. W. Kim and S. S. Kim, Grain-Size-Tuned Highly H_2-Selective Chemiresistive Sensors Based on ZnO–SnO_2 Composite Nanofibers, *ACS Appl. Mater. Interfaces*, 2016, **8**, 2486–2494.

62 R.-J. Wu, D.-J. Lin, M.-R. Yu, M. H. Chen and H.-F. Lai, Ag@SnO_2 core–shell material for use in fast-response ethanol sensor at room operating temperature, *Sens. Actuators, B*, 2013, **178**, 185–191.

63 S.-W. Choi, A. Katoch, J.-H. Kim and S. S. Kim, Remarkable Improvement of Gas-Sensing Abilities in p-type Oxide Nanowires by Local Modification of the Hole-Accumulation Layer, *ACS Appl. Mater. Interfaces*, 2015, **7**, 647–652.

64 C. S. Rout, A. R. Raju, A. Govindaraj and C. N. R. Rao, Hydrogen sensors based on ZnO nanoparticles, *Solid State Commun.*, 2006, **138**, 136–138.

65 L. F. Zhu, J. C. She, J. Y. Luo, S. Z. Deng, J. Chen and N. S. Xu, Study of Physical and Chemical Processes of H_2 Sensing of Pt-Coated WO_3 Nanowire Films, *J. Phys. Chem. C*, 2010, **114**, 15504–15509.

66 C. Liu, Q. Kuang, Z. Xie and L. Zheng, The effect of noble metal (Au, Pd and Pt) nanoparticles on the gas sensing performance of SnO_2-based sensors: a case study on the {221} high-index faceted SnO_2 octahedra, *CrystEngComm*, 2015, **17**, 6308–6313.

67 W. Xia, C. Mei, X. Zeng, G. Fan, J. Lu, X. Meng and X. Shen, Nanoplate-Built ZnO Hollow Microspheres Decorated with Gold Nanoparticles and Their Enhanced Photocatalytic

and Gas-Sensing Properties, *ACS Appl. Mater. Interfaces*, 2015, **7**, 11824–11832.

68 A. L. Zou, Y. Qiu, J. J. Yu, B. Yin, G. Y. Cao, H. Q. Zhang and L. Z. Hu, Ethanol sensing with Au-modified ZnO microwires, *Sens. Actuators, B*, 2016, **227**, 65–72.

69 X.-j. Wang, W. Wang and Y.-L. Liu, Enhanced acetone sensing performance of Au nanoparticles functionalized flower-like ZnO, *Sens. Actuators, B*, 2012, **168**, 39–45.

70 X. Li, X. Zhou, H. Guo, C. Wang, J. Liu, P. Sun, F. Liu and G. Lu, Design of Au@ZnO Yolk–Shell Nanospheres with Enhanced Gas Sensing Properties, *ACS Appl. Mater. Interfaces*, 2014, **6**, 18661–18667.

71 X. Liu, J. Zhang, L. Wang, T. Yang, X. Guo, S. Wu and S. Wang, 3D hierarchically porous ZnO structures and their functionalization by Au nanoparticles for gas sensors, *J. Mater. Chem.*, 2011, **21**, 349–356.

72 W. Tang, J. Wang, P. Yao and X. Li, Hollow hierarchical SnO_2-ZnO composite nanofibers with heterostructure based on electrospinning method for detecting methanol, *Sens. Actuators, B*, 2014, **192**, 543–549.

73 S. Wlodek, K. Colbow and F. Consadori, Signal-shape analysis of a thermally cycled tin-oxide gas sensor, *Sens. Actuators, B*, 1991, **3**, 63–68.

74 Y. Wang, B. Zhang, J. Liu, Q. Yang, X. Cui, Y. Gao, X. Chuai, F. Liu, P. Sun, X. Liang, Y. Sun and G. Lu, Au-loaded mesoporous WO_3: preparation and n-butanol sensing performances, *Sens. Actuators, B*, 2016, **236**, 67–76.

75 K. Arshak and I. Gaidan, Development of a novel gas sensor based on oxide thick films, *Mater. Sci. Eng., B*, 2005, **118**, 44–49.

76 M. Rafiqul Islam, N. Kumazawa and M. Takeuchi, Titaniumdioxide chemical sensor working with AC voltage, *Sens. Actuators, B*, 1998, **46**, 114–119.

77 Z. Feng, Y. Ma, V. Natarajan, Q. Zhao, X. Ma and J. Zhan, In-situ generation of highly dispersed Au nanoparticles on porous ZnO nanoplates via ion exchange from hydrozincite for VOCs gas sensing, *Sens. Actuators, B*, 2018, **255**, 884–890.

78 G. Henkelman, A. Arnaldsson and H. Jónsson, A fast and robust algorithm for Bader decomposition of charge density, *Comput. Mater. Sci.*, 2006, **36**, 354–360.

79 E. Sanville, S. D. Kenny, R. Smith and G. Henkelman, Improved grid-based algorithm for Bader charge allocation, *J. Comput. Chem.*, 2007, **28**, 899–908.

80 W. Tang, E. Sanville and G. Henkelman, A grid-based Bader analysis algorithm without lattice bias, *J. Phys.: Condens. Matter*, 2009, **21**, 084204.

81 K. H. Hong, G. M. McNally, M. Coduri and J. P. Attfield, Synthesis, Crystal Structure, and Magnetic Properties of $MnFe_3O_5$, *J. Inorg. Gen. Chem.*, 2016, **642**, 1355–1358.

82 L. P. Salamakha, E. Bauer, S. I. Mudryi, A. P. Gonçalves, M. Almeida and H. Noël, Isothermal section of the Ce–Au–Sb system at 870K, *J. Alloys Compd.*, 2009, **479**, 184–188.

83 Y. Chen, Y. Wei, P. Chang and L. Ye, Morphology-controlled synthesis of monodisperse silver spheres via a solvothermal method, *J. Alloys Compd.*, 2011, **509**, 5381–5387.

84 N. L. Tarwal, A. V. Rajgure, J. Y. Patil, M. S. Khandekar, S. S. Suryavanshi, P. S. Patil, M. G. Gang, J. H. Kim and J. H. Jang, A selective ethanol gas sensor based on spray-derived Ag–ZnO thin films, *J. Mater. Sci.*, 2013, **48**, 7274–7282.

85 Y. Wei, X. Wang, G. Yi, L. Zhou, J. Cao, G. Sun, Z. Chen, H. Bala and Z. Zhang, Hydrothermal synthesis of Ag modified ZnO nanorods and their enhanced ethanol-sensing properties, *Mater. Sci. Semicond. Process.*, 2018, **75**, 327–333.

86 J. Ding, J. Zhu, P. Yao, J. Li, H. Bi and X. Wang, Synthesis of ZnO–Ag hybrids and their gas-sensing performance toward ethanol, *Ind. Eng. Chem. Res.*, 2015, **54**, 8947–8953.

87 Q. Xiang, G. Meng, Y. Zhang, J. Xu, P. Xu, Q. Pan and W. Yu, Ag nanoparticle embedded-ZnO nanorods synthesized via a photochemical method and its gas-sensing properties, *Sens. Actuators, B*, 2010, **143**, 635–640.

88 X. Xing, X. Xiao, L. Wang and Y. Wang, Highly sensitive formaldehyde gas sensor based on hierarchically porous Ag-loaded ZnO heterojunction nanocomposites, *Sens. Actuators, B*, 2017, **247**, 797–806.

89 N. Hongsith, C. Viriyaworasakul, P. Mangkorntong, N. Mangkorntong and S. Choopun, Ethanol sensor based on ZnO and Au-doped ZnO nanowires, *Ceram. Int.*, 2008, **34**, 823–826.

90 L. Chengchao, L. Limiao, D. Zhifeng, Y. Hongchun, X. Yingying, L. Yuan, C. Yong and W. Taihong, Rapid and ultrahigh ethanol sensing based on Au-coated ZnO nanorods, *Nanotechnology*, 2008, **19**, 035501.

91 E. Wongrat, P. Pimpang and S. Choopun, Comparative study of ethanol sensor based on gold nanoparticles: ZnO nanostructure and gold: ZnO nanostructure, *Appl. Surf. Sci.*, 2009, **256**, 968–971.

92 J. Zhang, X. Liu, S. Wu, B. Cao and S. Zheng, One-pot synthesis of Au-supported ZnO nanoplates with enhanced gas sensor performance, *Sens. Actuators, B*, 2012, **169**, 61–66.

93 T. Santhaveesuk, D. Wongratanaphisan and S. Choopun, Enhancement of sensor response by TiO_2 mixing and Au coating on ZnO tetrapod sensor, *Sens. Actuators, B*, 2010, **147**, 502–507.

94 Z. Yuan, X. Jiaqiang, X. Pengcheng, Z. Yongheng, C. Xuedong and Y. Weijun, Decoration of ZnO nanowires with Pt nanoparticles and their improved gas sensing and photocatalytic performance, *Nanotechnology*, 2010, **21**, 285501.

